CANTED BLADES FOR A VERTICAL AXIS WIND TURBINE

POWER PERFORMANCE, FLOW BEHAVIOUR AND EXCITATION RESPONSE OF CANTED BLADES FOR A VERTICAL AXIS WIND TURBINE

By

SHAWN ARMSTRONG, B. Eng & MGMT / Co-op

A Thesis

Submitted to the School of Graduate Studies

in Partial Fulfilment of the Requirements

for the Degree

Master of Applied Science

McMaster University

© Copyright by Shawn Armstrong, February 2011

MASTER OF APPLIED SCIENCE (2011)	McMaster University
(Mechanical Engineering)	Hamilton, Ontario

TITLE:	Power performance, flow behaviour and excitation response of canted blades for a vertical axis wind turbine
AUTHOR:	Shawn Armstrong, B. Eng & MGMT / Co-op
SUPERVISOR:	Dr. Stephen Tullis
NUMBER OF PAGES:	xv, 87, A-1, B-7

ABSTRACT

The ability of vertical axis wind turbines to operate effectively in the presence of highly unstable, turbulent wind flow patterns makes them ideal candidates for small scale applications in urban environments, where erratic wind flow patterns are quite common. Their axisymmetric nature allows for wind energy extraction during conditions of rapidly varying wind direction, and their base mounted generator location permits relatively easy maintenance, making them a more suitable design for small scale urban installations as compared with traditional horizontal axis turbines. Wind tunnel experiments were carried out on a small scale, high solidity, three-bladed Darrieus wind turbine with canted (tilted) blades. The effects of preset blade pitch (β = +2.5°, -1.5°, -3.5° and -5.5°) and of aerodynamic fences were investigated at high Reynolds numbers (>500,000) for their effect on power performance while simultaneously characterizing the flow behaviour on a section of the inner blade surface using Mylar tufts and a shaft-mounted video camera. The excitation response of the turbine was also measured. The results are compared to a set of similar straight blades.

The results of pitching the canted blades show that the power performance increases up to C_{Pmax} = 0.28 for increasing outward blade pitch, to a best observed pitch of β = -3.5° after which the power performance decreases. Canted blades show acute sensitivity to inwards pitch where the power coefficient dropped to C_{Pmax} = 0.06 at β = +2.5°. The power coefficient observed for canted blades was C_{Pmax} = 0.29 at 9 m/s wind speed which was slightly higher than C_{Pmax} = 0.26 measured for the equivalent set of

straight blades that were tested at the same preset pitch (β = -3.5°) at 10 m/s wind speed. The maximum power coefficient occurred at a higher blade speed ratio for canted blades (λ = 2.15) compared to straight blades (λ = 1.7) despite nearly identical solidities (σ = 0.45 for canted blades versus σ = 0.43 for straight blades). Aerodynamic fences improve the power performance of canted blades to C_{Pmax} = 0.29 at 8 m/s wind speed to and C_{Pmax} = 0.31 at 10 m/s wind speed and reduce the speed at which peak power occurs to λ = 1.9. Aerodynamic fences do not noticeably change the power performance of straight blades.

Flow visualization using Mylar tufts attached to the inside blade surface indicated that canted blades experience reversed flow exclusively during the upwind pass of their rotation at peak power. Overall, canted blades experience less reversed flow than straight blades at the same blade speed ratio and only develop minor reversed flow during the downwind pass for blade speed ratios substantially below peak power where straight blades experience significantly more reversed flow. Aerodynamic fences further reduce the amount of reversed flow on canted blades, especially directly below the fence.

Due to differences in the peak operating speeds and the primary natural frequencies of the wind turbine with canted blades and straight blades, a direct comparison of the excitation response of canted blades and straight blades is not presently possible. However, normalizing the data suggests that canted blades do show reduced excitation response over straight blades.

This study shows that the current set of canted blades produces acceptable power levels, with the potential for further refinements to improve performance, and suggests that reduced excitation response can be achieved with canted blades.

ACKNOWLEDGEMENTS

I would not have made it to this point without my supervisor, Dr. Stephen Tullis. Not only did he offer me this unique research opportunity, but he also lent his knowledge and experience to my work while treating me like an equal and not a subordinate. I have thoroughly enjoyed my experience working with him and hope that many others will have the same opportunity in the future.

As the last researcher to join the vertical axis wind turbine group, a lot of work had been done before me on the turbine, the control system and the analysis procedures. I am grateful for the contributions of Stephen Tullis, Rafael Bravo, Kareen Aly, Stephen Kooiman, Kevin McLaren and Andrzej Fiedler for their efforts in this respect. Additional thanks are due for Kevin and Andrzej who helped with the experiments and the data processing.

I would also like to thank the faculty of the Mechanical Engineering Department for both my undergraduate and graduate education and the support they have offered me over the years. The Department technical staff has also been of great assistance, so a special thank you goes out to Ron Lodewyks, Mark McKenzie, Jim McLaren, Joe Verhaeghe, Dave Schick and J.P. Talon for their assistance.

The financial support from Ontario Centres for Excellence and from Cleanfield Energy made my research possible and I am grateful for it. I also wish to thank the estate of Raymond Moore for the scholarship support which allowed me to study and complete my research without having to worry about my personal finances.

My friends, family, and especially my girlfriend and parents have supported me throughout this endeavour. They gave me the space and support I needed when the workload was heaviest and I can't tell them how much I appreciate it.

TABLE OF CONTENTS

LIST OF FIGURES

LIST OF TABLES

NOMENCLATURE

English Characters

A_S	rotor swept (projected) area [m^2]
A_B	blade planform area [m^2]
c	blade chord length [mm]
C_P	power coefficient; non-dimensional ratio of turbine aerodynamic power to wind power
C_{Pmax}	maximum power coefficient (at peak power)
N	number of blades
P_{out}	output power [W]
P_{aero}	aerodynamic power [W]
R	radius [m]
Re_c	chord Reynolds number; $\rho c \lambda U\infty/\mu$
U	net incident wind velocity [m/s]
U_∞	undisturbed upstream wind velocity [m/s]
U_{rot}	wind velocity due to blade rotation [m/s]
x	location on blade measured along chord line from leading edge [mm]

Greek Characters

α	angle of attack; angle between the blade chord and the net incident wind velocity [°]
β	fixed preset blade pitch; angle between the blade chord and the tangent to the swept arc at the blade mount point [°]
θ	azimuthal angle [°]
λ	blade speed ratio; non-dimensional ratio of the blade speed to the undisturbed upstream wind speed
μ	air viscosity [kg/m·s]
ρ	air density [kg/m^3]
σ	solidity; non-dimensional ratio of total blade planform area to turbine swept (projected) area
ω	turbine angular velocity [rad/s]

Abbreviations

2D	Two dimensional
3D	Three dimensional
CFD	Computational fluid dynamics
NRC	National Research Council
RPM	Revolutions per minute

CHAPTER 1: INTRODUCTION

1.1 THESIS STATEMENT

A set of canted blades were designed and manufactured for a vertical axis wind turbine. The blades were tested experimentally at a wind tunnel to determine their power performance as well as the effects of preset (fixed) pitch change and aerodynamic fences on power performance. Vibration (excitation response) of the wind turbine with canted blades was also examined.

1.2 MOTIVATION

As energy demand continues to rise, government commitment and public desire to produce more of our energy from environmentally friendly sources, like wind, has also increased.

Horizontal axis wind turbines, so named because the axis of rotation is typically horizontal, are used almost exclusively in commercial power generation applications. The distinguishing characteristic of a horizontal axis wind turbine is that the blades are oriented perpendicular to the rotor rotational axis and accept axial flow. Vertical axis wind turbines typically have their blades parallel to the axis of rotation (which is perpendicular to the oncoming wind and usually vertical). Both types have advantages and disadvantages with respect to construction and operation.

Horizontal axis wind turbines operate most efficiently in areas where the wind speed and direction are relatively consistent, such as offshore, along shorelines or at

elevations sufficiently above surrounding obstacles. In areas where air flow patterns are more irregular and wind direction changes frequently and quickly, such as lower elevations or an urban setting, vertical axis wind turbines are better suited for operation because they do not need to be yawed into the wind like horizontal axis wind turbines. The starting point of the present study is an experimental turbine similar to the commercial Cleanfield V3.5, a small scale, high solidity Darrieus style vertical axis wind turbine, shown in Figure 1-1.

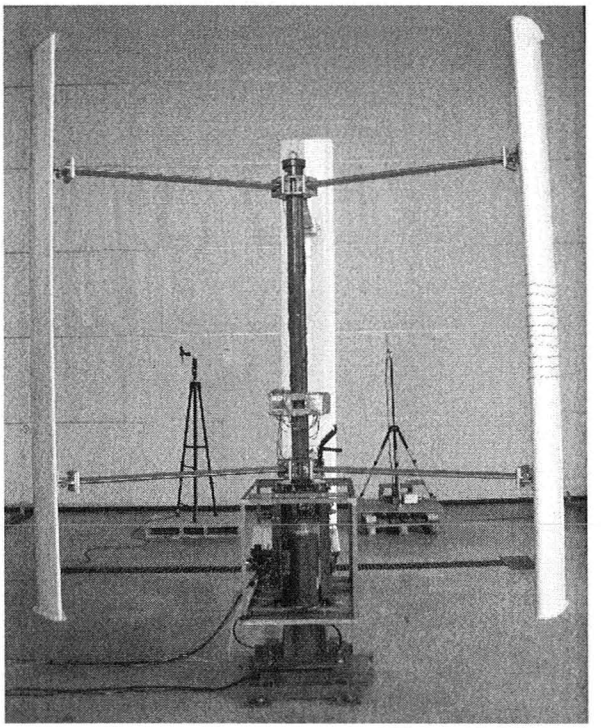

Figure 1-1: Experimental version of the Cleanfield high solidity H-Darrieus vertical axis wind turibne installed in the University of Waterloo Live Fire Research Facility.

Darrieus-style vertical axis turbines may be either troposkien or H-Darrieus type. A troposkien is an idealized shape formed by a mass-less flexible rope that is fixed at both ends (with a length longer than the distance between the fixed points) and spun about an axis formed by the fixed points. The resulting shape has purely tensile loading.

In practise, blades of this shape were approximated by straight line segments connected in the middle by a circular arc. H-Darrieus turbines use straight blades connected to the rotational axis with struts such that when viewed from the side the turbine resembles the letter *H* for the case of a single strut in the middle of the blade.

If a small scale vertical axis wind turbine is to be installed on a building, the structure must be strong enough to withstand the wind turbine loading levels during operation and resist fatigue due to cyclic aerodynamic loading. The tower (for a rooftop or stand-alone installation) cannot experience excessive vibration either. By reducing the net aerodynamic load fluctuations, the turbine components and tower can be designed to be less rigid which reduces material requirements and costs. The turbine lifespan is also increased and the operating costs are lower due to less vibration and reduced wear. The number of possible installation sites can also be expanded because the turbine can be installed on less stable structures. It is therefore the motivation of the present study to reduce the net aerodynamic load fluctuations while maintaining or increasing power output.

1.3 Objectives

The main objective of this research is to test a new set of canted blades, blades tilted at an angle to the vertical, for application on a vertical axis wind turbine, and to determine the power performance implications of replacing the straight blades with canted blades. Poor power performance of canted blades is unacceptable regardless of any improvement in the excitation response. Changes in the flow behaviour associated

with canted blades will also be examined using flow visualization. Secondary to the power output and flow behaviour, the operational excitation response of the wind turbine with canted blades installed will be compared to the equivalent straight bladed configuration. Although the motivation is to reduce the excitation response of the turbine, changes in the blade configuration (stiffness and mass) alone are likely to modify the response of the turbine structure such that a direct comparison may not be possible. Further operational differences could arise despite efforts to design the canted blades to operate as closely as possible to the straight blades, differences that would make a comparison even more challenging. Therefore, the excitation response will be examined in a context determined by the final operating parameters of the system, with the goal to get as best an indication as possible of how canted blades affect the turbine excitation response. Designing and testing another set of blades may be necessary for conclusive excitation response results, which is beyond the scope of the present work.

This is not the first attempt at changing the blade configuration of a vertical axis wind turbine to distribute aerodynamic load fluctuations. Helical blades were developed specifically for that purpose by Gorlov (1995), but manufacturing complexities substantially increase the cost of helical blades in comparison to straight blades. Canted blades are proposed here because they incorporate a linear axis like straight blades and can be manufactured in a similar manner to simple straight blades, while still offering the benefits of distributed aerodynamic loading. The impact of canted blades on power performance, flow behaviour and excitation response are studied in this thesis.

Aerodynamic flow conditioning devices - blade fences – are also examined for their effects on turbine power performance and flow behaviour.

1.4 Thesis Layout

This thesis is composed of five chapters comprising an introduction, three chapters outlining the research and a conclusion. The introduction discusses the motivation and objectives for the present research. Chapter 2 provides the reader with a technical background on vertical axis wind turbines as well as current review of literature related to the present research. Detailed descriptions of the design and manufacturing of canted blades, the experimental apparatus, the testing facility and the testing methods are presented in Chapter 3. Chapter 4 discusses the experimental results. Conclusions, a summary of the results and recommendations regarding further work on canted blades are included in Chapter 5.

Appendix A contains full coordinates for the airfoil and the aerodynamic fences. Error analysis is performed in Appendix B.

CHAPTER 2: BACKGROUND AND LITERATURE REVIEW

2.1 VERTICAL AXIS WIND TURBINE OPERATION

In most cases, the ultimate goal of operating a wind turbine is to produce electrical power. In absolute terms power output is measured in watts, however, to allow for comparisons between different turbine sizes and configurations, the power output is frequently reported as a non-dimensional power coefficient, C_P, given by:

$$C_P = \frac{P_{out}}{0.5\rho A_S U_\infty^3}$$

As there are often many components between the rotor of the turbine and the final electrical output, P_{out} may be defined in different ways. By considering P_{out} as P_{aero}, the net aerodynamic power of the turbine rotor, aerodynamic performance changes to the rotor can be isolated from other components in the system. P_{aero} is used in the present study. ρ is the air density, A_S is the rotor swept (or projected) area and U_∞ is the undisturbed upstream wind speed. C_P is plotted against the blade speed ratio, λ, defined as:

$$\lambda = \frac{U_{rot}}{U_\infty} = \frac{\omega R}{U_\infty}$$

where U_{rot} is the rotational speed of the blade, ω is the rotational rate and R is the radius, which gives the non-dimensional rotational speed of the turbine.

An additional non-dimensional parameter used to describe wind turbines is the solidity, σ, which is the ratio of the blade planform area, A_B, to the rotor swept area. Solidity can be simplified to:

$$\sigma = \frac{A_B}{A_S} = \frac{Nc}{2R}$$

for the case of a straight-bladed H-Darrieus turbine using the number of blades, N, the chord, c, and the radius, or to give the local solidity of canted blades. The optimal blade speed ratio of a turbine is related to its solidity as discussed later in Section 2.X.

To understand the fundamental operation of a vertical axis wind turbine, a simplified quasi-steady state analysis is instructive in which conditions like rotation rate and wind speed are assumed constant at a specific blade orientation for a short period of time. Figure 2-1 shows a section view of a typical vertical axis wind turbine.

As the turbine rotates, the blade experiences an air velocity due to rotation that is tangent to the blade path, U_{rot}. If there is no ambient wind, $U_\infty = 0$, the angle of attack, α, of is nominally 0°. A second air velocity is experienced by the blade if the ambient wind is non-zero. In this case, the rotational velocity and the wind velocity can be added as vectors to give the resultant air velocity, U, where the angle of attack will be non-zero except when the blade is travelling directly into (or away from) the wind. For non-zero angles of attack, a lift and a drag force will be produced on the blade, which can be resolved into radial and tangential components. The net tangential forces drive the turbine to produce power while the radial force on each blade is responsible for blade flexing and blade fatigue. The net loading on the turbine due to all radial and tangential

forces is composed of an average load and an excitation causing fluctuating load that together determine the turbine strength requirements and dictate fatigue resistance criteria.

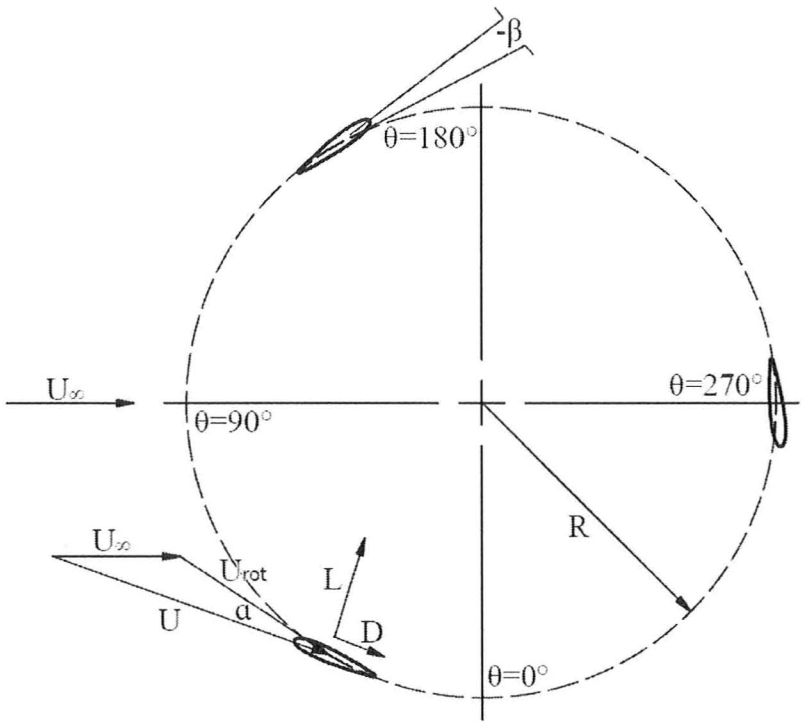

Figure 2-1: Section view of an H-Darrieus turbine showing the azimuthal angle, θ, incident wind, U_∞, wind due to rotation, U_{rot}, angle of attack, α, preset blade pitch, β, and the resulting lift, L, and drag, D, forces.

In generating power, the turbine extracts kinetic energy from the wind resulting in reduced wind speeds through and downstream of the turbine dictated by conservation of momentum. This flow retardation propagates upstream as well because the turbine acts as a pressure obstacle to the air flow, the extent to which is strongly dependent on the turbine solidity. Consequently, some of the air flows around the sides as well as above and below the turbine. The theoretical performance limit for wind turbines was based upon optimal flow retardation through the turbine. It was shown by Betz (van Kuik,

2007) that the maximum possible efficiency (C_{Pmax}) of a horizontal axis rotor modeled as a non-ducted, infinitely thin actuator disc with no drag losses or wake rotation in incompressible, axial flow is 16/27 (0.593). Since a vertical axis turbine has both an upwind and a downwind pass where energy can be extracted, Newman (1983) modeled a vertical axis turbine as a double actuator disc which he showed to have a maximum efficiency of $C_{Pmax} = 0.64$.

Using a quasi-steady analysis method, the resultant air velocity and angle of attack on the blade can be calculated for any azimuthal position, at which point lift and drag coefficients can be applied from static airfoil data to estimate the turbine power production and loading. This was the basis of Strickland's (1975) streamtube model and Paraschivoiu's (1981, 1983) double multiple streamtube model, both of which are iterative in nature, account for wind speed reductions through the turbine based on momentum transfer from the flow to the turbine, and are significantly more complicated than the simplified model presented here. The main difference between the two models is that the double multiple streamtube model incorporates an upwind and downwind pass. Both are limited in their predictive ability to lower solidity configurations with low chord-to-radius ratios, where the blades behave more as linearly translating singular points such that static airfoil data provides a reasonable approximation. Despite attempts to account for flow curvature (Mandal & Burton, 1994, Hirsch & Mandal, 1984, Migloire et al., 1980) and dynamic stall (Mandal & Burton, 1994, Paraschivoiu & Allet, 1988, Paraschivoiu & Delclaux, 1983) at higher solidities and higher chord-to-radius ratios, the

fundamental assumptions of the double multiple streamtube model limit its usefulness for high solidity turbines.

An alternative to streamtube models is to perform computational fluid dynamics (CFD) analysis on high solidity vertical axis turbines. McLaren et al. (2009, 2007) performed 2D CFD studies with full scale experiments and Howell et al. (2010) performed both 2D and 3D CFD studies on high solidity turbines in addition to experimental work to which the CFD was compared. Howell et al. (2010) and McLaren et al. (2009) found that the 2D CFD consistently over predicted the power output. This was due to the inherent ducting of 2D models which prevents flow expansion above and below the turbine, and, as Howell et al. (2010) noted from 3D simulations, the existence tip vortices that do not appear in 2D studies. Additional CFD studies have also been performed by Fiedler (2009), Hamada et al. (2008), Ferreira (2007a), Guerri et al. (2007), Hansen & Sorensen (2001) and Allet et al. (1999).

2.2 Power Performance of Vertical Axis Turbines

Predictive models and CFD simulations have been verified against experimental power measurements. Some of the earliest published work on vertical axis wind turbines was performed in the late 1970s and early 1980s by Sandia National Laboratories. The research focussed on lower solidity troposkien-style Darrieus turbines. Blackwell et al. (1976) tested a variety of solidities ranging from $\sigma = 0.13$ to $\sigma = 0.3$. Figure 2-2 shows Blackwell et al. (1976) data for $\sigma = 0.13$ and $\sigma = 0.3$. The optimal blade speed ratios were $\lambda = 5.6$ and $\lambda = 4.0$, respectively.

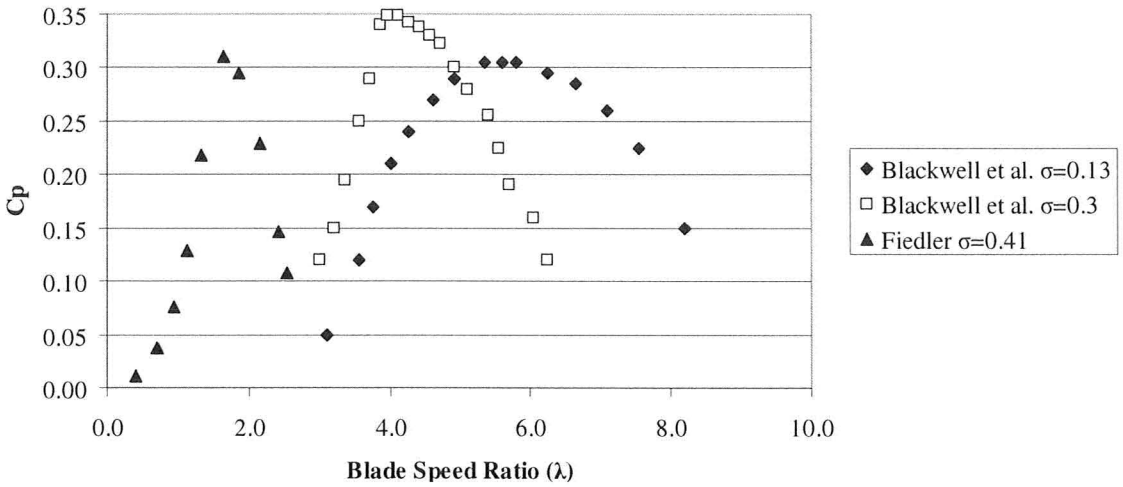

Figure 2-2: Power coefficient data for the Sandia 5m troposkien wind turbine with NACA 0012 airfoils (Blackwell et al., 1976) at different solidities and the 3m H-Darrieus turbine with NACA 0015 airfoils (Fiedler, 2009).

More recently, power performance data has been published by Bravo et al. (2007) and Fiedler et al. (2009) on high solidity H-Darrieus type turbines that were nearly identical the straight-bladed turbine used in the present study. Bravo et al. (2007) tested the straight-bladed turbine at the National Research Council of Canada wind tunnel where the blockage ratio at the 9m x 9m tunnel was 10% and Fiedler (2009) tested a nearly identical turbine at the Waterloo Live Fire Research Facility where the blockage was 20%. The results of the two series of tests compare well and due to the similarity, only the Fiedler (2009) data is shown in Figure 2-2. Bravo et al. (2007) observed a peak power coefficient of $C_{Pmax} = 0.29$ while Fiedler (2009) achieved a peak power coefficient of $C_{Pmax} = 0.32$, which is comparable given the small changes to the struts, blade pitch and loss accounting methods between the two series of tests. The peak power blade speed ratio was about $\lambda = 1.6$ for both. Bravo et al. (2007) noted that, at the NRC tunnel, the power coefficient became independent of Reynolds number above $Re_c = 4x10^5$ (wind

speed of 8 m/s) while Fiedler (2009) saw Reynolds number independence at about Re_c = $5x10^5$ (wind speed of 10 m/s).

2.3 Blade Pitch Effects

Changing the angle of attack for a simple static airfoil in a fluid flow results in altered lift and drag forces, therefore the angle of attack or pitch of a wind turbine blade should have an impact on the turbine performance. Some wind turbines incorporate passively or actively controlled pitching mechanisms to improve power output or induce stall for turbine protection and power regulation. Almost all vertical axis turbines use fixed pitch blades, so to maximize energy capture an optimal preset pitch must be used, with consideration of both the upwind and downwind passes. The pitch angle, β, as defined in Figure 2-1, is positive for toe-in (leading edge inwards) configurations since this increases the angle of attack on the upwind pass.

Experiments by Sound and Rangi (1972) on a low solidity (σ = 0.07) Darrieus turbine showed that changing the preset pitch from β = -4° to β = -0° resulted in an 11% increase in C_{Pmax}. While this would seem to indicate that toe-out pitch impaired performance, it is possible that an optimal pitch existed between the two pitches tested. On a σ = 0.22 solidity turbine tested by Klimas and Worstell (1981), power increases were seen for toe-out pitch equivalent blade offsets up to β = -2° followed by decreases beyond β = -2°. Klimas and Worstell (1981) tested pitch equivalent offsets of β = +3°, +1°, -0.5°, -2°, -4° and -7°. Theoretical predictions by Paraschivoiu (2002) regarding

preset pitch showed the same trends. In light of the available literature, it is expected that pitch will be an important performance parameter for canted blades.

More recently, Fiedler's (2009) work on the pitch effects on a high solidity vertical axis turbine showed that an optimal, toe-out fixed pitch exists up to which point increasing the toe-out pitch yields performance improvements. Fiedler's pitch effects are shown in Figure 2-3. After the optimal pitch is reached, any further toe-out leads to diminished performance. Fiedler (2009) achieved $C_{Pmax} = 0.32$ at a blade speed ratio of $\lambda = 1.63$ and pitch of $\beta = -6°$. The turbine used three straight blades with 400mm chord length NACA 0015 airfoils and had a height of 3.0m and diameter of 2.95m. The solidity was $\sigma = 0.41$. Fiedler's (2009) results also showed acute sensitivity to toe-in pitch resulting in significantly worse performance. Fiedler (2009) also investigated the effects of blade mounting offset from mid-chord. A given offset is geometrically equivalent to a corresponding pitch, and it was shown that offset and pitch are also aerodynamically equivalent such that mounting offset can be compensated by the analogous pitch. Due to the similarities in turbine size, airfoil and chord, canted blades were expected to give a similar power output to Fiedler's (2009) straight blades. Fiedler's work can be considered as a base case or starting point for the present work given the similarities in the turbine components used and overall dimensions of the turbine and airfoils.

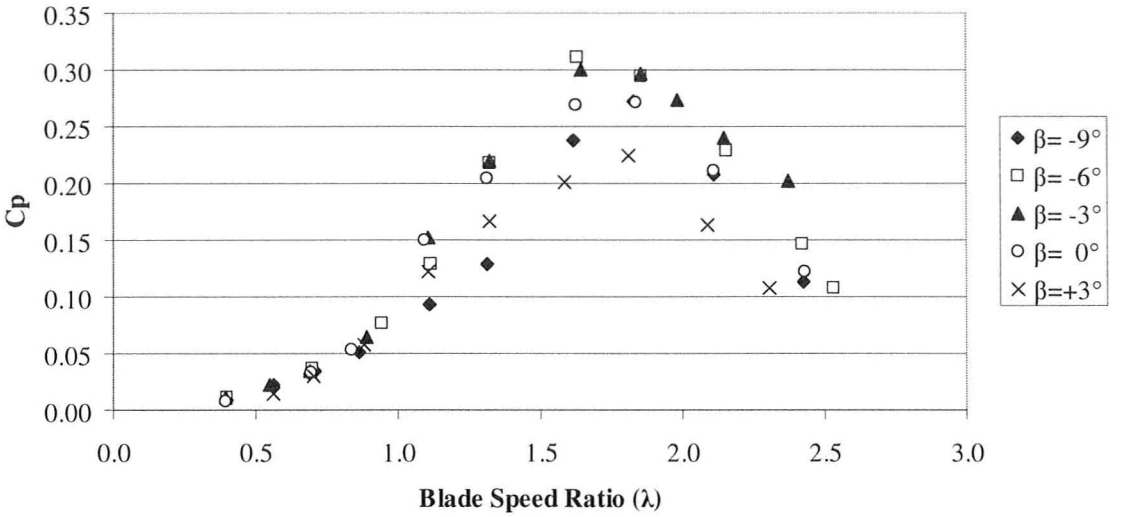

Figure 2-3: Power coefficient data for the Fiedler 3m H-Darrieus turbine at various preset pitches. $Re_c = 5.0x10^5$ at $\lambda = 1.6$.

2.4 Flow Visualization on Vertical Axis Wind Turbines

The validation of CFD models has also been based on detailed comparisons with different forms of flow visualisations and measurements. Early tests were performed by Strickland et al. (1979) in a water towing tank using trailing edge dye injection to observe the wake. The model spanned nearly the entire tank depth attempting to create 2D flow and was tested in one-, two- and three-bladed configurations, giving solidities of σ = 0.075, 0.15 and 0.225, respectively. The dimensions of the turbine resulted in a 21% blockage ratio and Reynolds number of Re = 40,000. Blade-vortex interactions were difficult to see using the trailing edge dye.

Brochier et al. (1986) performed similar water tunnel testing of a two-bladed Darrieus turbine at a Reynolds number of Re = 10,000 with a solidity of σ = 0.33. This model also spanned the entire tunnel depth but the blockage ratio was substantially higher

at 60%. Laser-doppler velocimetry and flow visualisation were used measure velocity profiles and observe flow patterns. Measurement details were given for blade speed ratios of $\lambda = 2.14$ and $\lambda = 3.85$, which were estimated to be below and above peak power. At a blade speed ratio of $\lambda = 2.14$, it was shown that dynamic stall was important whereas it was less so at the higher blade speed ratio. The continued interaction of a blade with its shed vortices was observed into the downwind pass at a blade speed ratio of $\lambda = 2.14$.

Particle image velocimetry (PIV) and flow visualisation measurements were done by Fujisawa and Shibuya (2001) on a single-bladed turbine of solidity $\sigma = 0.167$. The blockage ratio was 40% and due to the limited velocity the Reynolds number was only Re = 3,000. Vortex shedding and blade-vortex interactions were sketched for blade speed ratios of $\lambda = 1, 2, 3$, where $\lambda = 3$ was estimated to be close to peak power.

More recently Ferreira et al. (2009, 2007b) published PIV results of testing a single-bladed $\sigma = 0.125$ turbine in a wind tunnel at Re = 50,000 and Re = 70,000. The single straight blade had an aspect ratio of 20 and was mounted in a 2D configuration between two rotating discs with an in-plane blockage ratio of 32%. The PIV data showed the development of dynamic stall on the upwind suction side of a NACA0015 airfoil, with a particular focus on the leading edge separation vortex and trailing edge shed vorticity, and was used to validate CFD models by the same authors. Additional work by Ferreira et al. (2008) involved the use of a two-bladed turbine with a solidity of $\sigma = 0.21$ to achieve a Reynolds numbers of about Re = 100,000. Very limited PIV data was presented, and only for the single blade speed ratio of $\lambda = 2$ at a single azimuthal angle of $\theta = 20°$.

Flow visualization was also recently used by Fiedler (2009) to qualitatively investigate the flow patterns on the inside (suction) surface of a straight blade on a turbine with a solidity of $\sigma = 0.41$ at a number of preset pitches. The technique involved recording video footage of an array of Mylar tufts affixed to the inner surface of the blade in such a manner that allowed normal or reversed flow to be identified. Tufts (lightweight string, thread, Mylar strips) have been used extensively as visual indicators of flow behaviour and patterns on surfaces (often wings and blades) and are particularly useful when conditions are not steady. It was found that increasing the blade speed ratio delayed the initial appearance of reversed flow and reduced the azimuthal range over which maximum reversed flow was observed. More negative preset pitch, from $\beta = 0°$ to $\beta = -6°$, also tended to delay the first appearance of reversed flow and reduce the azimuthal range of maximum flow reversal while for further outwards pitch an increase in flow reversal was observed.

2.5 Helical Blades

Despite the limitations of the 2D CFD simulations in predicting power output, the load curves can be used as estimates of the turbine loading. Figure 2-4 shows theoretical load curves produced by a 2D CFD simulation by McLaren et al. (2009) of a three-bladed high solidity turbine. The forces are shown for each of the three blades, which vary depending on the blade azimuthal position, θ, and for the net load produced by all three blades, which is approximated well by a sinusoidal function with a frequency three times the rotation speed.

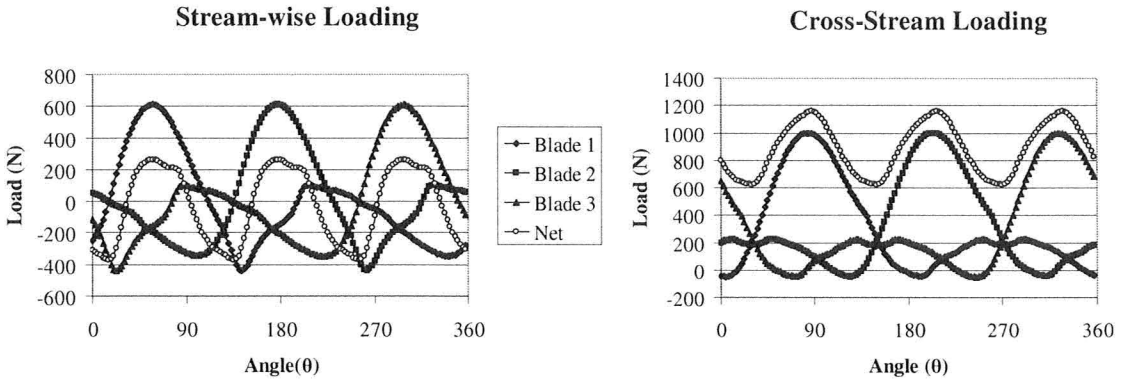

Figure 2-4: Theoretical loads on a three-bladed high solidity H-Darrieus turbine based on CFD simulations by McLaren et al. **(2009).**

If the load amplitude of a single blade and the net load amplitude are compared, it can be seen that increasing the number of blades would have a smoothing effect on the loads. Therefore adding more blades is an effective method of reducing net load fluctuations. Continuing to add blades is not practical from a cost, structural or efficiency standpoint. Alternately, the turbine could be cut in half at the waist and the top and bottom staggered by 60°, resulting a six, albeit shorter, blade configuration. If the turbine was cut twice with each section staggered by 30°, then the load would be smoothed over nine blades. Gorlov (1995) realized that in the limit the result of this procedure would be a helix, and so he proposed and patented a turbine with helical blades. This allowed a segment of each blade to occupy a fraction of the circular path traced by the blades, ideally so that a portion of blade occupies every part of the circle, eliminating the net effect of aerodynamic fluctuations. While elegant in design, a helix is a complicated, highly three-dimensional object with no linear or planar sections. It is consequently challenging to manufacture objects of this geometry even at small scales, with obvious additional complications as size increases. For composite fabrication common to the

wind industry, machining moulds for such blades is a time, labour and cost intensive operation due to the non-linear geometry, and it would be difficult to establish a suitable single parting plane. Alternately, blade fabrication using internal plugs requires that new plugs be precisely milled for each blade even before fibre can be laid up. These procedures are definitely more complex, time consuming and expensive than for conventional planar composite fabrication. Therefore in this thesis canted blades are proposed to address the practical shortcomings of helical blades.

2.6 Swept Wings

Both canted blades and helical blades bear some similarity to swept wings while straight blades behave more like straight wings. In the late 1940's, once the benefits of swept wings for high speed flight had been realized, NACA and later NASA performed a considerable amount of research on various properties of swept wings at both low and high speeds.

Some of the earliest reported work on swept wings from NACA detailing the aerodynamic effects of sweep was performed by Letko and Goodman (1946). Their model consisted of two rectangular wings with NACA 23012 sections and could be configured for sweep angles of Λ = 0°, 30°, 45° and 60°. Results showed that at low speeds for increasing angles of sweepback, the slope of the linear portion of the lift curve was reduced, maximum lift was delayed to higher angles of attack and stall occurred more gradually. Maximum lift was higher at Λ = 30° sweepback than for no sweep with some additional drag while lift at Λ = 45° and Λ = 60° was less. Similar results were

shown by Purser and Spearman (1951) for NACA 0015 airfoils tested at Λ = 0°, 30° and 60° sweepback. Given the high angles of attack experienced by the present high solidity turbine, these characteristics should be beneficial for canted blades.

The primary concern in using swept wings for aircraft was a sudden loss of lift due to stall at the wing tips resulting in an abrupt pitching moment that initiated further pitch-up, stall propagation and loss of aircraft control due to flow separation over the ailerons. Tip stall was mostly caused by spanwise flow along the wing that resulted in a thicker boundary layer at the wing tips making them more susceptible to stall at lower angles of attack and lower lift coefficients than for comparable straight wings. This was particularly problematic at low speeds during landing.

Several aerodynamic flow control devices were tested with the goal of improving longitudinal stability by preventing spanwise flow and tip stall. These included vortex generators, leading edge extensions and wing fences. At low speeds, fences were shown to be effective at increasing the section lift coefficients of a swept wing while reducing drag considerably at high lift coefficients (Cleary and Boddy, 1953). A minor drag increase was seen at low lift coefficients. Tests were performed with two fences installed at 50% and 65% wingspan locations, and five fences installed at 20%, 35%, 50%, 65% and 80% wingspan locations, which showed that the highest number of fences was most effective in increasing the lift coefficient of the outermost sections of the wing while the innermost sections showed slightly lower lift coefficients.

A variety of tests were performed by Queijo et al. (1952?) on a Λ = 35° sweptback wing using multiple fence configurations to determine the effects of fence length, height

and shape. It was shown that fences with lengths as short as 0.26c could be used with little reduction in effectiveness compared to the longest fence (0.80c) tested in the particular series. Further testing showed that except for very low fences, changes in fence height had little impact on fence effectiveness. For one of the better fences tested, the maximum fence height was 0.051c. Queijo et al. also found that the shape at the rear part of the fences was relatively unimportant given a sufficient fence length and extension of the fence (0.018c) beyond or around the leading edge. If substantial spanwise flow is present on the canted blades, fences may help to improve performance.

St. Hilaire et al. (1979) conducted a study to determine the effect of sweep on the aerodynamic loading of an oscillating NACA 0012 airfoil. The tests were performed at the 2.44m octagonal United Technologies Research Center Main Wind Tunnel using a 40.6cm chord model that spanned the tunnel and was capable of $\Lambda = 0°$ and 30° sweep angles. Frequencies tested ranged from four to ten cycles per second. For both swept and unswept configurations, the mean incidence angle and pitching amplitude were tested at a number of different values such that the blades operated unstalled, between stall and no stall, and fully stalled. It was found that sweep tended to delay the onset of dynamic stall. Furthermore, sweep reduced the magnitude of the unsteady lift and pressure drag relative to their mean response. These effects are similar to the delayed and moderated stall behaviour for static airfoil tests on swept wings.

Recent studies using CFD for high solidity vertical axis wind turbines (McLaren et al., 2009, Howell et al., 2010, Fiedler, 2009) showed considerable dynamic stall was present especially at low blade speed ratios. Given the moderating effect of sweep on

dynamic stall shown by St. Hilaire et al. (1979), it is expected that canted blades should benefit with similar load smoothing.

CHAPTER 3: EXPERIMENTAL APPARATUS

The experimental apparatus consists of a base turbine (generator, shaft, struts, bearings, instrumentation), canted blades, straight blades and aerodynamic modifications (blade fences and pitch adapters). Full scale testing was carried out at a wind tunnel. These components, the test facility and the analysis procedures are discussed in this chapter.

3.1 CANTED BLADE DESIGN

All experiments detailed in this study were performed using components from prototype and production versions of a Cleanfield V3.5 vertical axis wind turbine. The V3.5 is an H-Darrieus with a height of 3.0m and a diameter of 2.87m that uses three blades equally spaced at 120°. The projected area of the V3.5 is 8.61m^2, solidity is σ = 0.44 and chord-to-radius ratio is 0.29. The blades were each attached to the central shaft with two support struts located 675mm from the blade ends. For testing purposes, the central shaft could also operate in a 180° two-blade configuration.

For the present study, the straight blades and canted blades both used symmetric airfoils. Typically, NACA 0012 or NACA 0015 profiles have been used, however, the production blades on the V3.5 use a profile closer to that of a NACA 0013 airfoil. The profile of the straight blades is based on a 450mm chord NACA 0015 which is shortened to 420mm by rounding the trailing edge. Airfoil coordinates can be found in Appendix A. This was done due to manufacturing limitations in achieving consistent dimensions of a sharp trailing edge. A small slice was also taken out along the chord line to allow for a

glue gap, which, in practise, ended up being too large so that the assembled blade has a thickness of about a NACA 0013 with a chord of 420mm. The mounting point of the blades was 150mm from the leading edge.

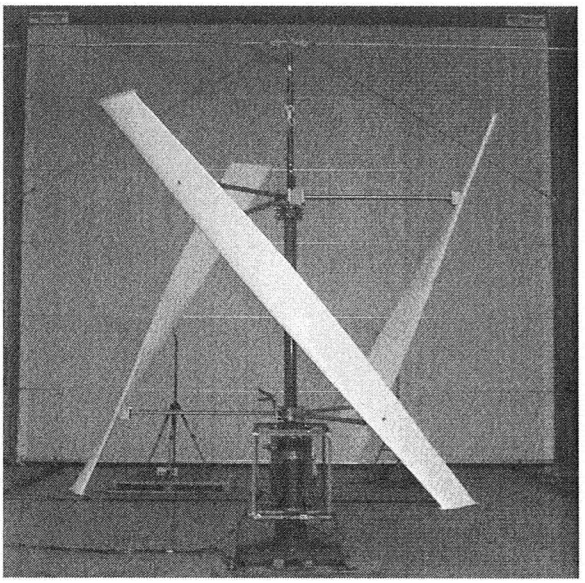

Figure 3-1: Experimental turbine with canted blades installed. The cant angle is 40° from vertical.

For comparability, the same modified NACA 0015 airfoil was used on the canted blades. A canted blade was made by tipping or "canting" a straight blade forward about its center to angularly offset the top and bottom of the blade. A US Provisional Patent, Serial No. 61/310,970 [2010], has been filed regarding canted blades. The blades in this study were canted 40° from vertical to use mounting points displaced by $\theta = 60°$ and separated vertically by 1710 mm. By canting the blades, the local blade pitch relative to the rotational axis changed, so the blades were also twisted about their axes to maintain constant pitch. To maintain turbine height, the blades were lengthened approximately 40%. Another result of canting the blades is a variable radius, with the top and bottom having larger radii than the "waist" of the turbine. Due to the variable radius, which is a

trigonometric function of the cant angle, the local blade speed is not constant along the blade, and, as discussed in Section 3.2, careful attention was required to attempt to match the local solidity to the local blade speed ratio for power performance reasons. The canted blades are shown installed on the experimental turbine structure in Figure 3-1.

A manufacturing approach similar to the current process used for straight blades was applied to the canted blades where two fibre-glass skins were bonded at the leading and trailing edges and in the middle with spars that can be seen in Figure 3-2. The skins for the canted blades were laid up in female molds machined in medium density fibre-board. The asymmetric nature of the blade (not the airfoil) made it necessary to have unique molds for the inner and outer skin. Two square C-channel spars were borrowed from the straight blades and cut down the middle because the C was too high for certain sections of the canted blades. With the inner skin sitting in its mold, one half of each C-channel was twisted and glued to the inner surface of the skin. Once the glue had set, the other half of each C-channel was twisted and glued to the first half. A round C-channel was glued in pieces – in pieces because it was not easily twisted – along the leading edge. The trailing edge was relatively flat and could be glued without any additional reinforcements. A CNC milled ash (wood) insert was glued to the inner surface of the skin in which a ball joint was embedded to serve as the mount point of the blade. Glue was then applied along the trailing edge and the mating sections of C-channels immediately before the outer skin was placed on top of the assembly. Using existing spars kept the costs lower for the prototype build but reduced the blade strength, particularly near the inserts where most of the spars had to be trimmed away to

accommodate the insert. Any production canted blade would need custom spars and different inserts which would greatly improve the blade strength.

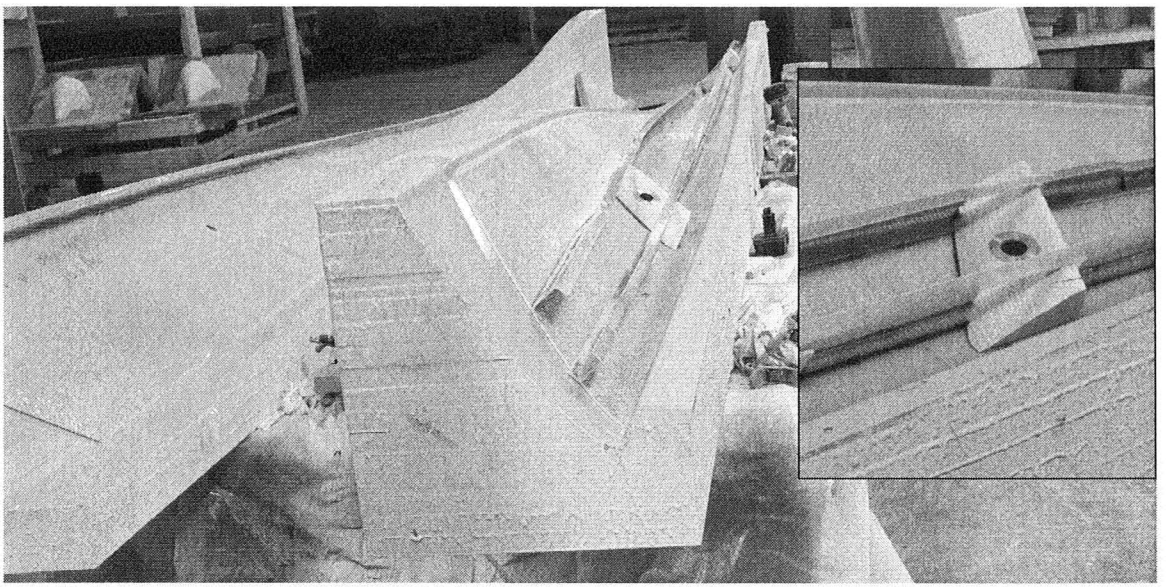

Figure 3-2: Manufacturing of canted blades showing the inner skin sitting in the mould with spars and ash insert glued in place.

Due to the angular offset between the top and bottom of the blade, each blade wraps approximately 90° around the turbine for a total wrap of 270°. For an ideal helical turbine, each of three blades would wrap 120°. A 120° wrap may not be ideal for canted blades, since the wrap of a canted blade varies along its length due to the variable radius. The wrap follows a trigonometric tangent curve resulting approximately half the wrap angle for a given blade element at the tips as compared to at turbine waist. This variable wrap accentuates the aerodynamic loading differences and should act to more effectively smooth load fluctuations. Figure 3-3 shows a schematic top view of the turbine with canted blades installed showing the wrap of the blades.

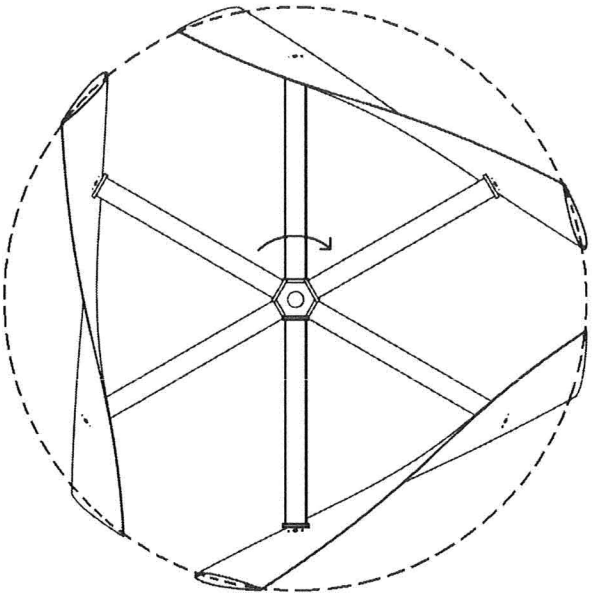

Figure 3-3: Top view of the turbine showing the approximately 270° wrap of the canted blades.

Figure 3-4 shows the effect of solidity on peak blade speed ratio where a number of optimum blade speed ratios are plotted against their solidity. The data was adapted from tests conducted by Blackwell et al. (1976) and by South and Rangi (Paraschivoiu, 2002). Figure 3-4 also includes tests performed by the present author using a variant of the present straight bladed turbine with and without spacers at the end of the struts and in a two-blade configuration to cover a range of solidities. In general, the peak power blade speed ratio decreases as the turbine solidity increases. At low solidities, the optimal blade speed ratio trends appear to be roughly inversely proportional to the solidity while at higher solidities the curves flatten out. Both the Blackwell et al. (1976) and South and Rangi (Paraschivoiu, 2002) rotors were troposkien in shape while the current tests were performed on a straight-bladed turbine. For a troposkien turbine, the blade speed ratio (tip speed ratio) is reported at the point of largest diameter, located at the middle of the

turbine where the radius is largest, and is similar to tip speed ratios reported for horizontal axis wind turbines. Most of the blade is traveling at lower speeds than the "tip" on a troposkien turbine whereas the entire straight blade travels at the same speed for an H-Darrieus like the Cleanfield V3.5. Furthermore, since solidity is the ratio of the total blade planform area to the rotor projected area, for a troposkien rotor, a large fraction of the blade planform does not contribute to the power output and acts more like the support struts on an H-Darrieus. For the Blackwell et al. (1976) data, if the straight sections of the troposkien approximation are considered as struts, the blade planform and swept area are reduced, with the net effect of reducing solidity by 59%. This is shown as adjusted Blackwell et al. (1976) data in Figure 3-4. With this adjustment, the troposkien and straight configuration trends match much more closely.

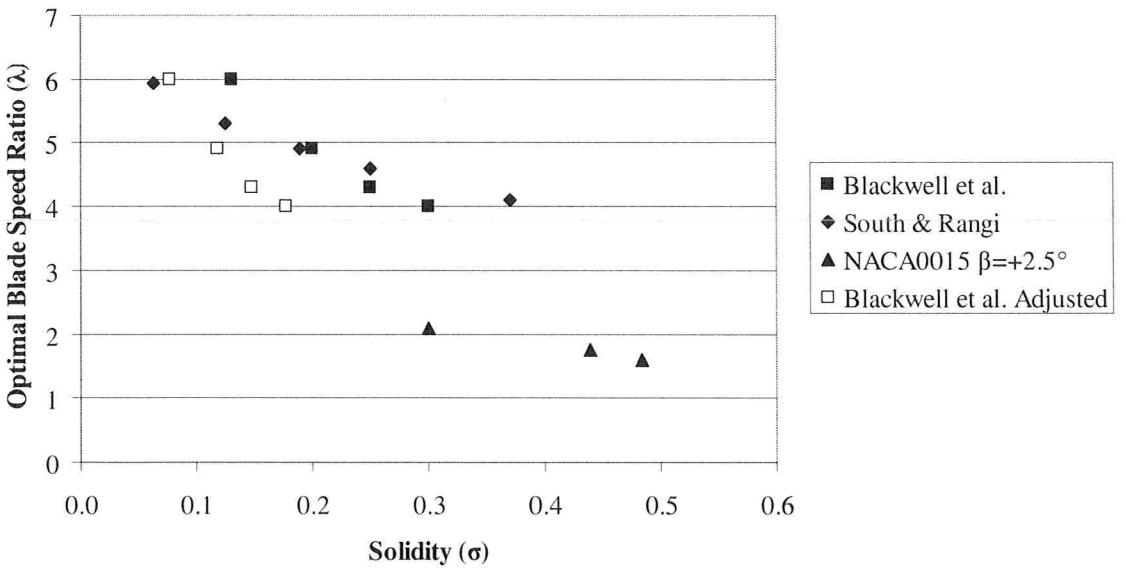

Figure 3-4: Optimal blade speed ratios for a number of solidities for vertical axis turbines.

The local blade speed along a canted blade is not constant due to the variable radius, therefore the local solidity must be carefully chosen to ensure peak performance is

reached simultaneously along the whole blade. Based on the data presented in Figure 3-4, an "optimal" solidity versus blade speed ratio trend was estimated for the canted blades. The corresponding local chord lengths were determined according to the constraint that the chord at the strut must be 420mm (modified 450mm) for comparability with the straight bladed turbine. Figure 3-5 shows the variation of radius, chord and solidity along the canted blades, as well as the radius and solidity of the straight blades used for comparison. As Figure 3-5 illustrates, the solidity of the canted blades was highest at the waist of the turbine where the radius and blade speed ratio were lowest. The overall solidity of the canted blades is σ = 0.45 which is slightly higher than the straight blade solidity of 0.43.

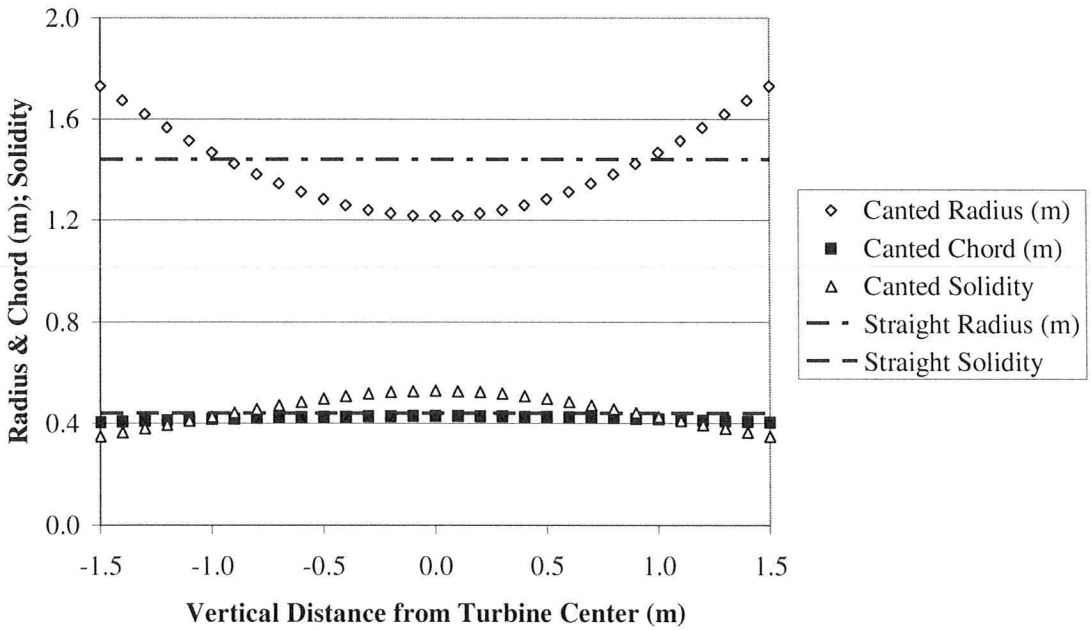

Figure 3-5: Radius, chord and local solidity variations of canted blades and straight blades.

3.2 Other Turbine Components

Components of the turbine other than the blades include the struts, shaft and generator, which were provided by Cleanfield and are shown in Figure 3-6. The struts are streamlined aluminum extrusions with rectangular plates welded to each end, where one end attaches to the blade and the other to the shaft. The strut profile is roughly elliptical with an aspect ratio of about 3 and a height of 37mm. The struts connect to the shaft at hexagonal sections that are 200mm flat-to-flat and separated vertically by 1650mm. The shaft consists of an inner stationary steel post and an outer freely rotating tube to which the blades attach. The generator has a similar construction as the shaft, such that the rotor spins around a stationary core (stator). When installed, the stationary component of the shaft is bolted to the stator while a torque coupler is used to connect the rotor to the shaft outer tube. For the duration of the tests, the generator circuit was kept open and no electrical power was extracted. In the event of a control system failure, the three phases of the generator could be shorted to bring the turbine to a reasonably fast, soft stop. The generator was mounted on a 0.75m high steel pedestal and frame that housed the instrumentation and control components.

An additional hexagon was manufactured from steel channel and mounted above the top hexagon on the shaft to allow mounting of the canted blades since the original shaft was not designed to accommodate offset struts at the top and bottom. This increased the vertical spacing of the struts for the canted blade case to 1710 mm.

Included in the frame control components was a Leeson C182-D17FK3 DC electric motor. Except in rare cases, the turbine would not self start so the motor was

used to bring the rotational speed past the lower operational threshold. The motor was connected to the generator via a friction drive belt that was driven by a pulley with a built in freewheel mechanism that allowed the motor to disconnect when not in use.

Two Kistler 8704B50 accelerometers were mounted near the top of the shaft, one to measure excitation in the same direction as the air flow (stream-wise) and one to measure transverse (cross-stream) excitation, cross-stream.

3.3 Turbine Control and Data Analysis

The turbine was controlled with a closed-loop proportional controller using a pulse width modulated signal based on the turbine rotational speed in revolutions per minute (Bravo et al., 2007). To calculate the rotational speed, a TURCK model Ni-4-M12-APX6-H1141 capacitive proximity sensor was mounted near the bottom of the generator where six equally angularly spaced bolt heads activated the sensor as they passed it during operation.

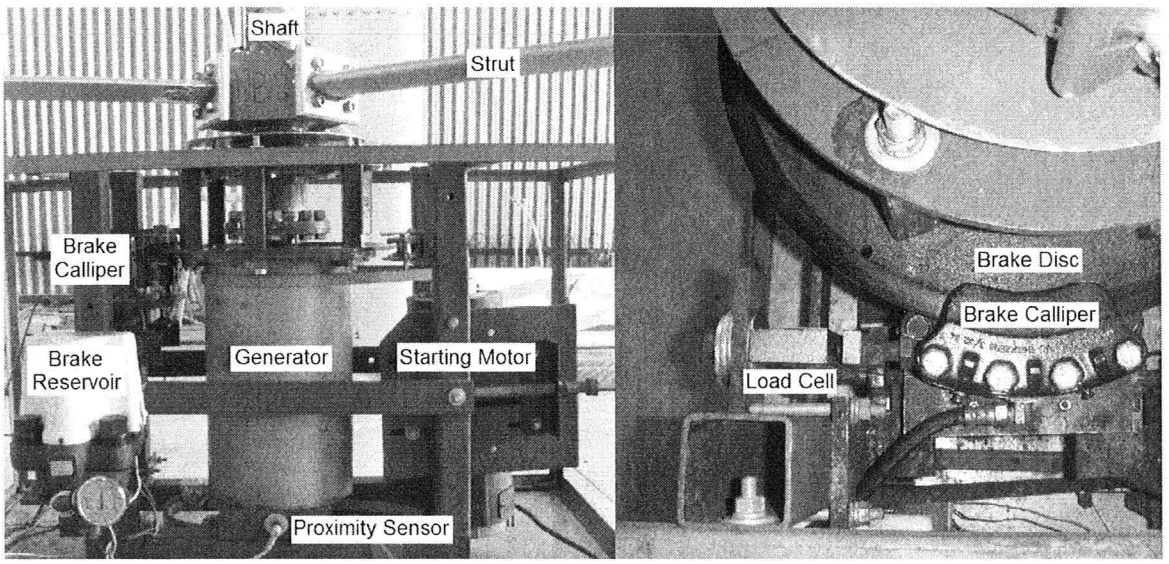

Figure 3-6: Lower portion of the turbine showing the generator, control system and instrumentation.

A large, steel brake disc was sandwiched between the generator rotor and torque coupler, as a means of applying torque to control the turbine. A disc brake calliper was installed on the frame using horizontally oriented pillow block bearings that allowed the calliper to translate tangent to the brake disc and on vertical bushings that allowed it to translate perpendicular to the disc surface. In this configuration, it was restrained radially and floated on the disc surface. Tangential restraint was provided by a Transducers Inc. #T363-500-20P1 load cell that was used to take torque measurements. The turbine speed was regulated with a modified, electrically controlled, hydraulic trailer brake actuator (BrakeRite model 5237006) that actuated the brake calliper. The brake actuator was modified by Fiedler (2009) who over-bored its solenoid control valve to lower the minimum operating pressure which significantly improved turbine control. In this configuration, all mechanical power at the shaft was taken out through the brake calliper via the load cell.

All control components were connected to an 8-channel National Instruments NI-DAQ 6015 data acquisition board and subsequently to a computer running custom NI Labview software. The software calculated the rotational speed from the proximity sensor and based on the difference between the desired and actual rotational speed, sent an appropriate PWM signal to the brake actuator.

30 second samples of wind speed at 10Hz and of load and rotational speed at 100Hz were recorded for each power performance data point. Torques and rotational speeds were multiplied to arrive at instantaneous output powers for the turbine that were subsequently averaged over the data sample. Power coefficients were based on the

averaged instantaneous wind powers during each sample interval. Losses were added back to the gross power measured to arrive at the aerodynamic power coefficient. Wind speed was measured three radii (4.2 m) upstream of the shaft. The procedure used for calculating the losses is discussed in Section 3.8.

The data from the accelerometers was sampled at 2048Hz, with 30 second data samples being recorded at all but the lowest rotational speeds (RPM <60) where 60 second data samples were taken to ensure a minimum of 30 rotations were captured (necessary for other unrelated measurements). A fast Fourier transform was applied to the samples to analyze the data in the frequency domain using eight second 50% overlapping sample blocks and applying a Hamming windowing technique. The final data is presented as power spectral density.

3.4 Test Facility

All tests were performed at the University of Waterloo Live Fire Research Facility (Devaud, 2004), the same facility used for Fiedler's (2009) experiments. The Live Fire Research Facility uses six Howden-Buffalo model 76-26 Series 1000 axial vane fans arranged in a two-high by three wide configuration to provide air flows of up to 11m/s. The fans are rated at 74.6kW (100HP) with a diameter of 1.98m (78") and draw air from outside the building. The fans form part of a plenum chamber that is approximately 8m long by 8m wide by 6m high, with two settling screens located 3.6m downstream of the fans and rectangular straightening ducts located at the plenum exit. The testing area is a large barn-like building with walls and ceiling more than 4m away

from the edge of the flow and large bay door at the rear of the building serving as an outlet, and is essentially an open flow tunnel. The turbine was placed in the center of the flow 8m downstream from the straightening grate, where a flow characterization study of the facility showed that a 5m high by 8m wide area had relatively consistent flow speeds with variations less than +/- 1m/s (Devaud, 2004).

The blockage ratio with the turbine (for both straight and canted blades) is 21% based on the turbine projected area and the local 8m by 5m flow section measured without the turbine present.

A set of six aircraft cables was used to stiffen the turbine structure via a steel extension tube mounted to the top of the shaft. The tube had a diameter of 51mm and was 1.3m long with ring at the end where the cables were attached. All cables were adjusted so that the tension was very nearly the same in all cables.

3.5 Blade Pitch

As mentioned previously, the canted blades were twisted to maintain constant local pitch of the blades, otherwise the excessive toe-out pitch at the upper tip and toe-in pitch at the lower tip would cause poor performance. Small changes in the blade pitch, such as those observed by Fiedler (2009), were also expected to have significant impacts on performance. Canted blades have a linear axis about which they can be pitched. A ball joint was incorporated at each strut connection to allow the blades to be accurately pitched simply by changing a retaining wedge between the blade and the strut. The wedges were made of spruce and CNC milled to match the blade contour for four

specified fixed pitches of β = +2.5° -1.5°, -3.5° and -5.5°. Figure 3-7 shows a CNC milled wedge installed between the blade and the strut.

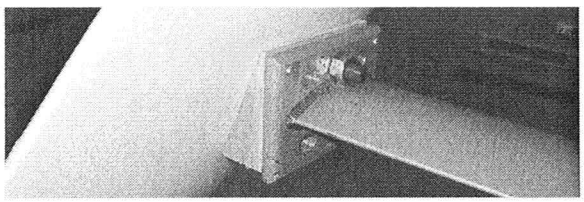

Figure 3-7: Canted blade and pitch wedge connected to a strut. Pitch was changed by replacing the pitch wedges between tests.

Due to mounting limitations, further toe-out pitch could not be accommodated on the present setup. The stated pitches were adjusted to report effective pitch to account for the off-center mounting location. Without correction, the mounting point, 150 mm from the leading edge on the 420 mm chord, resulted in a pitch of β = +2.5° with respect to the turbine shaft for the case where the pitch was β = 0° as measured with respect to the strut. The straight blades used CNC milled aluminum blocks to pitch the blades at a single pitch of β = -3.5°.

3.6 Blade Fences

It was expected that substantial spanwise flow may develop on canted blades based on early NACA and NASA testing of swept wings. A set of blade fences was fabricated according to dimensions outlined by Quiejo et al. (1954) to test the effect of operating canted blades with fences. The fences were installed in four different configurations on the canted blades. Fences were equally spaced and installed in multiples of either two or five fences, located on either only the inside (nearest the shaft) of the blade or on both the inside and outside of the blade. On the upwind blade pass

where most of the power is extracted, the inside is the suction side of the airfoil, which corresponds to the upper surface of a wing where fences were typically mounted on aircraft. Figure 3-8 shows the fence mounting locations and Table 3-1 shows a test matrix for fences. Fences were installed exclusively on the inside for the two- and five-fence cases, and on both sides for the four- and ten-fence cases.

Table 3-1: Test matrix for fences on canted blades

		Plane 1		Plane 2		Plane 3		Plane 4		Plane 5	
Blade	Case	In	Out	In	Out	In	Out	In	Out	In	Out
Canted	2F			✓				✓			
	4F			✓	✓			✓	✓		
	5F	✓		✓		✓		✓		✓	
	10F	✓	✓	✓	✓	✓	✓	✓	✓	✓	✓
Straight	5F	✓		✓		✓		✓		✓	

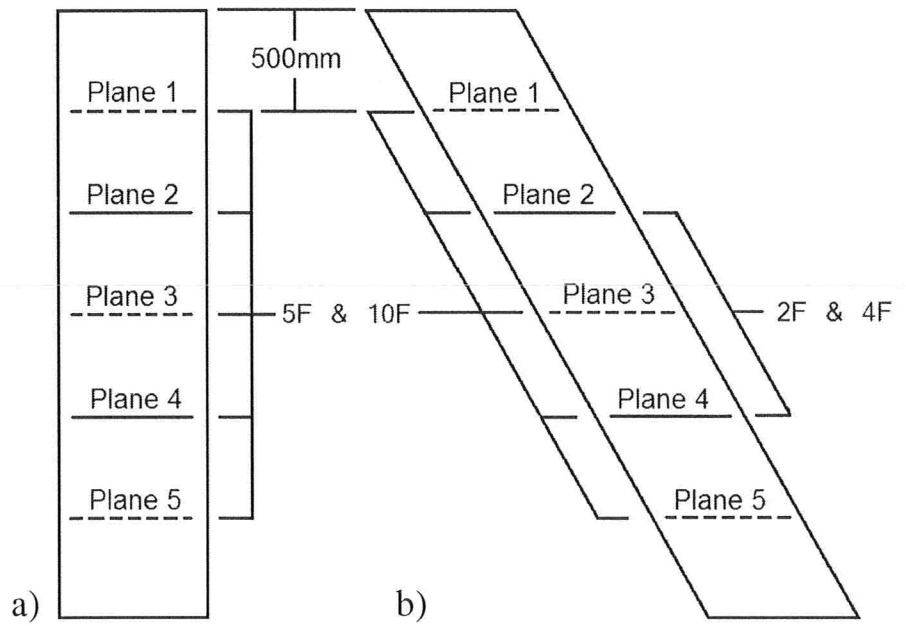

Figure 3-8: Blade fence installation locations on the a) straight blade and b) canted blade

The fences were CNC cut from 3/16" acrylic, the same material as the endplates on the blade tips. They extended 0.025c beyond the leading edge, had a maximum height

of 0.048c and terminated at 0.75c. Figure 3-9 shows the fence and airfoil profile of the canted blades along with an additional NACA 0015 airfoil that was used for flow visualization, which is discussed in the subsequent section. Due to the varying chord along canted blades, the absolute size of the fences varied with mounting location. Full coordinates for the fences can be found in Appendix A. A similar set of five inside fences was tested on the straight blades to quantify drag effects.

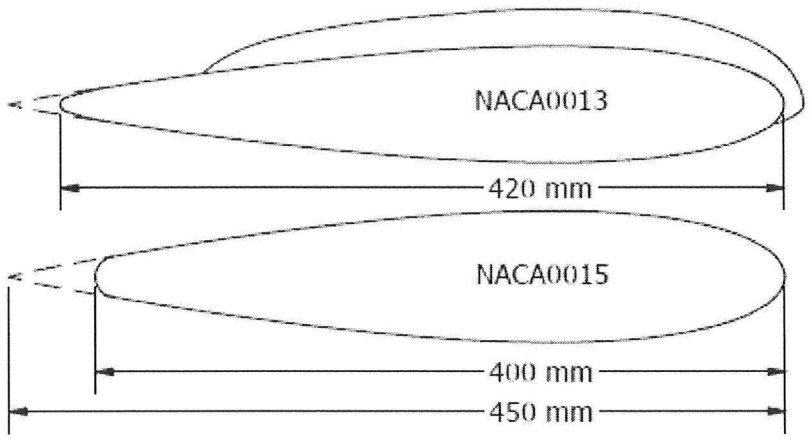

Figure 3-9: Blade fence shown to scale relative to the NACA 0013 airfoil used on the canted blades and the NACA 0015 airfoil used in the straight blade tuft visualization.

3.7 TUFTS

Arrays of bi-colour Mylar tufts were placed on the canted blades and on a different set of straight blades for flow visualization. Fiedler (2009) produced the tuft data for the different set of straight blades, which were similar to the straight blades used for present performance comparison except that they were a true NACA 0015 profile. Their chord was however shorter at 400mm as they were rounded off at a different

location. The profiles of the canted blades with a fence and the 400mm chord NACA 0015 profile are shown together in Figure 3-9.

The present tufts were approximately 5mm wide and 30mm long and were attached using clear adhesive tape to the inside surface of the blade. The free length of the tufts was about 25mm while 5mm was covered with the tape. The light and flexible nature of the Mylar allowed fast response of the tufts when subjected to rapid changes in flow direction and little effect due to centripetal acceleration, while the bi-color feature was useful in identifying the tuft orientation, attached or reversed. The tuft arrays are shown in Figure 3-10.

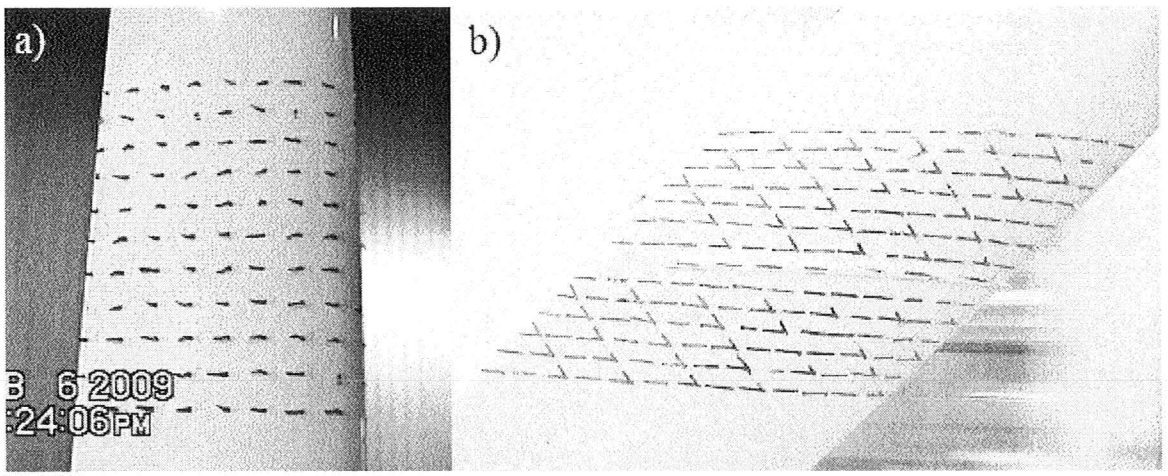

Figure 3-10: Tuft arrays on the (a) straight blade (Fiedler,2009) and (b) canted blade.

A Sony DCR-TRV30 video camera was mounted to the turbine shaft facing radially outwards at the turbine blade. The field of view was centered approximately 500mm below the middle of the turbine for both blade types, corresponding to fence plane 4. The focus and zoom were set to capture the tuft behaviour as clearly as possible while still allowing features in the background to be used as azimuthal location

references. The camera recorded video at 30 frames per second, which resulted in a number of frames per revolution that varied with rotational speed. Frame by frame visual analysis was performed on still images exported from the video. A storyboard of at least four rotations was compiled for each blade speed ratio at each pitch. In each still image, the number of separated tufts was counted and divided by the total number of tufts in the array, a number which represents the flow reversal fraction or separation fraction for the particular azimuthal position. The progression of flow reversal was also characterized by chord position to identify where reversal began, how it propagated and where reversed flow terminated. Centripetal force caused the camera to lose focus above 130 RPM during the straight blade tests, which corresponded to a blade speed ratio of $\lambda = 1.6$ for 10m/s wind speed. The mounting orientation was slightly different for the canted blades so focus was not a problem for canted blades.

3.8 Losses

Losses due to friction in the shaft and generator bearings and aerodynamic drag of the struts were accounted for using the method developed by Fiedler (2009) who performed an extensive series of tests on the starting motor of the turbine so that an accurate efficiency curve was available. With the blades removed from the turbine, the starting motor was used to drive the turbine through the entire operating range of rotational speeds in increments of approximately 20 RPM. At each speed, the power to the motor was measured and applied to the efficiency curve to calculate the losses due to drag and bearing friction. Depending on the configuration, pitch adapters or pitch

wedges were connected to the end of the struts to account for their additional drag. During the loss tests, the leading edge of the exposed outer surfaces of the pitch wedges (or blocks) cause flow separation that does not occur when the wedges are attached to the blades. This situation is similar to the difference between drag on a free rectangle versus a rectangle attached to a wall. The drag coefficient on a two dimensional free rectangle with a height-to-length ratio of 3 (as is approximately the case for the wedges and blocks) is C_D = 1.3 (Shaughnessy et al, 2005) whereas the same rectangle attached to a wall inside a turbulent boundary layer has a drag coefficient of about C_D = 0.9 (Holmes, 2003) in the range of Reynolds numbers tested, a 30% difference. The drag difference should not be so large presently because the wedges are quite close to the leading edge of the blade such that the boundary layer would be much thinner and because of the three dimensional effects of flow around the top and bottom of the wedges, which would reduce the drag difference to about 15%. Furthermore, the wedges (and blocks) only represent a fraction of the aerodynamic drag, so the effects of exposed outer wedge surfaces are likely less than 10% of the measured losses.

All loss tests were conducted in still air. This is not the flow encountered by the struts and wedges during normal operation, but provides a consistent measure for the losses since it would be difficult to recreate the exact flow conditions inside the turbine. The calculated losses using still air are lower than what would be calculated with wind so this method does not overestimate the losses and therefore does not artificially inflate power performance and likely offsets the 10% overestimate due to the wedges have exposed outer surfaces. Once the losses were included in the power measurement, power

coefficients were calculated by dividing the average power output by the average instantaneous wind power during the sample.

Power losses for the canted blade and straight blade configurations are shown in Figure 3-11. The geometry differences between pitch wedges and pitch blocks were responsible for the higher losses of the straight blades since the pitch blocks were quite large and their larger projected area caused significantly increased drag at higher speeds where aerodynamic losses dominate. At lower speeds the losses were similar in value and due mostly to friction losses in the shaft bearings.

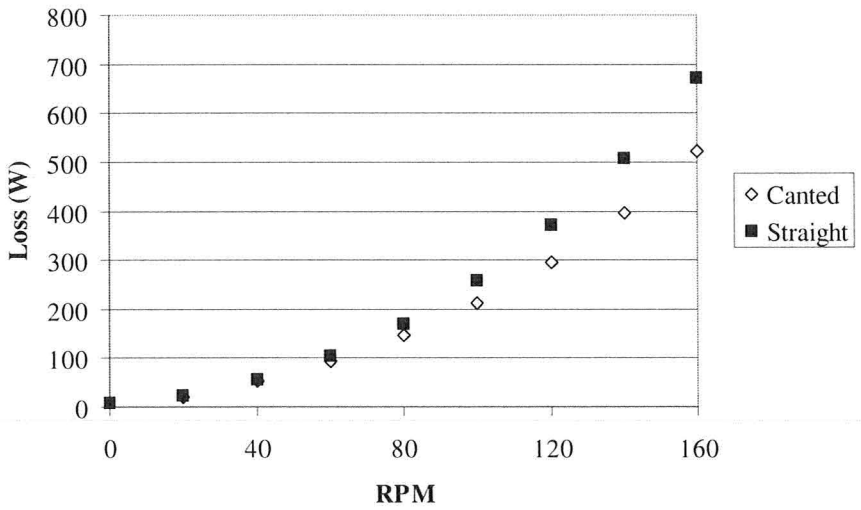

Figure 3-11: Power losses for straight blade and canted blade configurations determined by still air motor driven power requirements.

CHAPTER 4: RESULTS

Full scale experiments were conducted in an open-air wind tunnel to characterize the aerodynamic performance and excitation response of a newly designed set of canted blades and compare the results against comparable straight blades. Results are presented for power performance, excitation response and flow visualization.

4.1 POWER PERFORMANCE AND COMPARISON TO STRAIGHT BLADES

An extensive series of wind tunnel tests were performed on the turbine with canted blades installed. A range of fixed pitches and wind speeds were tested, as well as a number of different fence configurations. Most testing was carried out at wind speeds of 8 m/s as the canted blades were prototypes and their strength was not equivalent to a production version mostly due to the means by which the internal spars were installed. All data are presented as non-dimensional power coefficients that represent the net aerodynamic power of the turbine rotor, not the electrical power produced by the generator so the observed performance changes reflect differences in aerodynamic behaviour not differences in generator or inverter efficiencies.

The sources of error in the power performance data include the measurement of the wind speed, the torque and the rotational speed. Errors in the blade speed ratio are less than 8% at all wind speeds and account for 95% of the uncertainty. The placement of the anemometer due to the spatial variation in wind speed and the interpretation of the static load cell calibration were the largest sources of error in the power coefficients. At 8 m/s wind speed for canted blades operating near peak power, the error in the power

coefficients is +/-34%. At 10 m/s wind speed for canted blades with five fences operating near peak power, the error in the power coefficients is +/-31%. These errors account for 95% of the uncertainty in the measurements. An alternate, dynamic load cell calibration method could appreciably reduce the uncertainty in the torque measurements from the current levels. Also, the test facility has high turbulence levels associated with the non-uniformity in the flow so most of the wind speed error arises from attempting to represent a non-uniform flow by a single point measurement. The wind measurement errors are likely less than those included in these error values since the wind power is averaged over long time intervals (minimum 30 seconds) and is averaged spatially over the area of the turbine. Since the load cell calibration and anemometer placement affected all test cases similarly, the errors of 34% and 31% should be considered when comparing the subsequent data to external results. The repeatability of the present data is much better than the absolute errors such that the power coefficients are repeatable to 95% within a range of ΔC_P = +/-0.014 assuming a normal distribution and is shown later in Figure 4-3 where canted blades and straight blades are compared. Details of the error analysis can be found in Appendix B.

Figure 4-1 shows the effect of changing the fixed pitch of the canted blades at a constant 8m/s wind speed. The performance increased as the leading edge of the blade was pitched outwards to β = -3.5° where C_{Pmax} = 0.28 and diminished when further toe-out pitch was applied to β = -5.5° where C_{Pmax} = 0.26. The blade speed ratio at peak power was λ = 2.15. There is also an indication of an increase in the peak power blade speed ratio with increasing outward pitch. The performance was very sensitive to toe-in

pitch, which markedly decreased power output to $C_{Pmax} = 0.06$ for a pitch of $\beta = +2.5°$ at which point the blade speed ratio was also significantly lower at $\lambda = 1.7$.

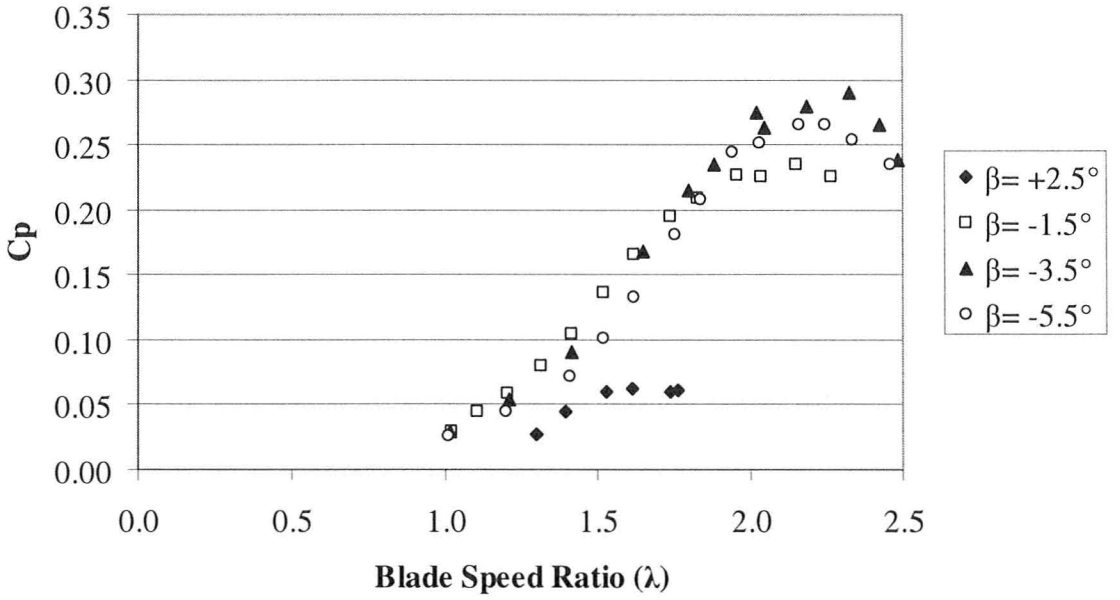

Figure 4-1: Power coefficient curves for canted blades showing the effect of pitch. Reynolds number at $\lambda = 2.15$ is 5.5×10^5. Wind speed is 8 m/s for all cases.

The effect of pitch on power performance can be explained in the same way as Paraschivoiu (2002) and Fiedler (2009) using a quasi-static analysis of the angles of attack seen by the blades. Flow deceleration through the upstream and downstream rotor passes as energy is extracted from the wind is considered in this approach. The angle of attack seen by the blade varies with azimuthal position depending on the relationship between the blade rotational velocity relative to the local wind speed (the instantaneous local blade speed ratio). On the upwind rotor pass, the local wind speed is high since no energy has been extracted from the flow leading to very high angles of attack. On the downwind pass where a significant amount of energy has been removed from the flow by

the upwind pass, the wind speed is lower while the blade velocity is unchanged resulting in quite low angles of attack. Pitching the blades outwards reduces the potentially excessive angle of attack on the upwind pass while simultaneously increasing the potentially too low angle of attack on the downwind pass. A mismatch between the optimum angles of attack on the upwind and downwind passes leads to the reduced peak power coefficients that are seen for the neutral, toe-in and excessively toe-out pitches as compared to the β = -3.5° pitch case.

The changes in the peak power blade speed ratio can be similarly explained. The optimal overall pitch is not necessarily the optimal pitch of the either the upwind or downwind pass independent of the other. Therefore, an incremental change in the pitch at any given preset pitch may improve the performance of one pass at the expense of the other, resulting in a different optimal operating point. The double multiple streamtube model of Paraschivoiu (2002) indicated that the optimal blade speed ratio of the upwind pass is higher than that of the downwind pass, so the shift of the peak power blade speed ratio to higher values for increased toe-out pitch suggests that more toe-out pitch favours the upwind pass or is unfavourable for the downwind pass.

A pitch of β = -3.5° was used to assess the performance of canted blades at different wind speeds since this pitch produced the highest power coefficient. These tests essentially present the effect of Reynolds number on the turbine performance. Reynolds number changes with azimuthal position, so the average Reynolds number is usually reported based only on the rotational velocity. Canted blades are further complicated by a variable blade speed ratio along the blade span due to the variable radius. For

comparability with straight blades, the Reynolds number, as with blade speed ratio, is reported where the blade is attached to the strut. Due to the variable radius and variable chord, Reynolds number was 1.17 times larger at the tips and lower by a factor of 0.89 at the waist compared to at the strut attachment point.

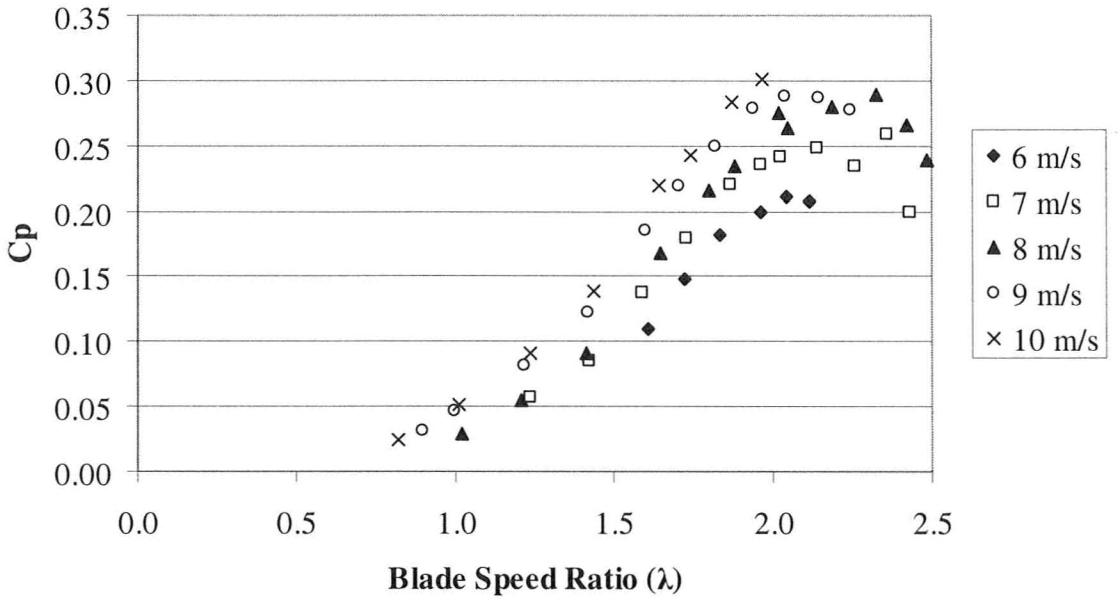

Figure 4-2: Power coefficient curves for canted blades showing the effect of wind speed. Pitch is β = -3.5° for all cases. 10 m/s curve is incomplete due to speed limitations of prototype canted blades.

Figure 4-2 shows how the performance of the canted blades changed at different wind speeds tested. The peak blade speed ratio was independent of the wind speed at about $\lambda = 2.15$. At 9 m/s, Reynolds number was $Re_c = 6.2 \times 10^5$ and peak power was only slightly higher at $C_{Pmax} = 0.29$ compared to 8m/s where $Re_c = 5.5 \times 10^5$. The 10m/s curve was incomplete due to strength and speed limitations of the prototype canted blades. but performance appears only slightly higher than 9 m/s. The maximum power coefficients were reduced at lower wind speeds, down 11% to $C_{Pmax} = 0.25$ at 7 m/s and lower by 25% to $C_{Pmax} = 0.21$ at 6 m/s where Reynolds number effects were prominent.

The convergence of the power coefficient above $Re_c = 5.5x10^5$ (8 m/s) is significant because previous testing of a similarly sized straight-bladed vertical axis turbine by Bravo et al. (2007) to higher Reynolds numbers (higher wind speeds) at the NRC wind tunnel showed a similar collapse of power coefficient curves above approximately $Re_c = 4.0x10^5$. Testing by Fiedler (2009) at the Waterloo facility showed a similar collapse around $Re_c = 5.0x10^5$. The higher Reynolds number required for power independence of canted blades is most likely due to sweep. If the velocity component perpendicular to the blade is considered, the Reynolds number at 9 m/s would be Re_c $4.8x10^5$. Reasonable power performance conclusions can therefore be made between non-dimensional power curves for canted blades so long as the wind speed is a minimum of 8 m/s. Care should still be taken when comparing between different wind speeds since the 10 m/s, 9 m/s and 8 m/s curves do not collapse identically, suggesting that there is still a small amount of Reynolds number dependence.

Figure 4-3 shows a direct comparison between the performance of canted blades and equivalent straight blades. Both canted and straight blades are shown tested at a pitch of $\beta = -3.5°$. To minimize any effects from Reynolds number dependence, the data is presented for the highest Reynolds numbers available, $Re_c = 6.2x10^5$ (9m/s) for the canted blades and $Re_c = 5.5x10^5$ (10m/s) for the straight blades. The canted blades performed slightly better, achieving $C_{Pmax} = 0.29$ compared to $C_{Pmax} = 0.26$ of the straight blades. The pitch of the straight blades may not be optimal, as Fiedler (2009) observed slightly higher performance at $\beta = -6°$, where the power coefficient was higher by about

ΔC_P = 0.02. The peak power coefficient of the straight blades and canted blades can be considered essentially equivalent.

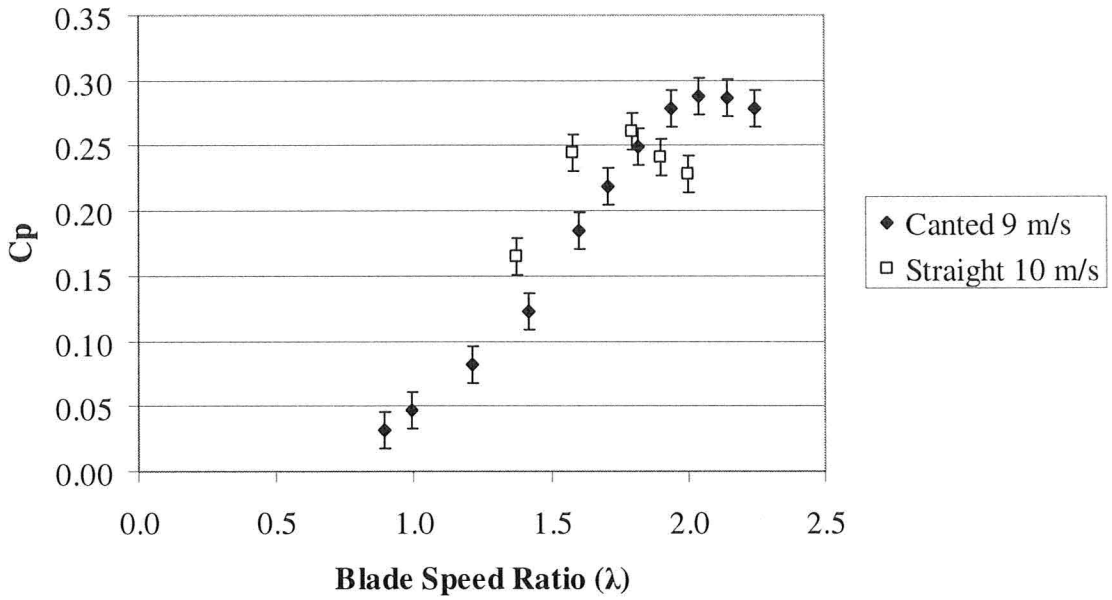

Figure 4-3: Power coefficient curves for straight blades and canted blades at β = -3.5°. Wind speed is 9 m/s canted blades and 10 m/s for straight blades. Error bars indicated repeatability to 95%.

The most significant difference between the two types of blades is the value of the peak blade speed ratio, λ = 1.7 for the straight blade compared to λ = 2.15 for the canted blades, with the canted blades operating roughly 25% faster than the straight blades. This is somewhat surprising since the solidity of the canted blades, σ = 0.45, is practically the same as that of the straight blades, σ = 0.44, and solidity is one of the most important determinants of optimal blade speed ratio. Furthermore, at the struts where the blade speed ratio is referenced, both blades configurations have identical radii and chord lengths. Therefore, it should be expected that canted blades operate at the same blade speed ratio as straight blades. The difference in operating speeds can be attributed to the same factors affecting the aerodynamic characteristics of swept wings used on aircraft.

Applying simple sweep theory to a canted blade, the incident flow can be resolved into a component flowing over the blade perpendicularly to its axis and a second component flowing spanwise along the axis. The resolved component of the incident wind (multiplied by the cosine of the cant angle) flowing perpendicularly over the canted blade is responsible for lift and power generation and is reduced through due to the cant angle. Therefore the canted blade must spin faster to achieve the same velocity perpendicular to the blade axis as an equivalent straight blade. The ideal sweep theory predicts a 30% speed increase for a sweep angle of $\Lambda = 40°$, which is roughly the same as the 25% increase in optimal blade speed ratio observed for the canted blades.

There are likely some differences between the straight blades and canted blades due to the differences in the airfoil thickness of approximately NACA 0013 for the canted blades and NACA 0015 for the straight blades. Substantially thicker airfoils show reduced dynamic stall effects and operate at slightly slower optimal blade speed ratios, however, given the small difference in airfoil thickness between the canted blades and straight blade any performance changes due to airfoil thickness are insignificant in comparison to the effects of canting the blades.

Fences were tested on the canted blades in different configurations at a pitch of $\beta = -3.5°$ and at 8m/s wind speed. Figure 4-4 shows the power coefficient curves for the various configurations of fences tested. The addition of two inboard fences reduced the peak blade speed ratio to around $\lambda = 2.0$ while the power coefficient remained unchanged at $C_{Pmax} = 0.28$. Increasing the number of inboard fences to five decreased the optimal blade speed ratio further to $\lambda = 1.9$ and increased the power coefficient by 7% to $C_{Pmax} =$

0.30. It is also clear from Figure 4-4 that the outboard fences in the four and 10 fence cases had little impact on the operating speed or power output compared to just the inboard 2 or 5 fences, however, tests with only outboard fences were not performed. It appears that the fences were acting to reduce spanwise flow on the canted blades such that when the fences were installed, the canted blades operated at a blade speed ratio nearer that of straight blades.

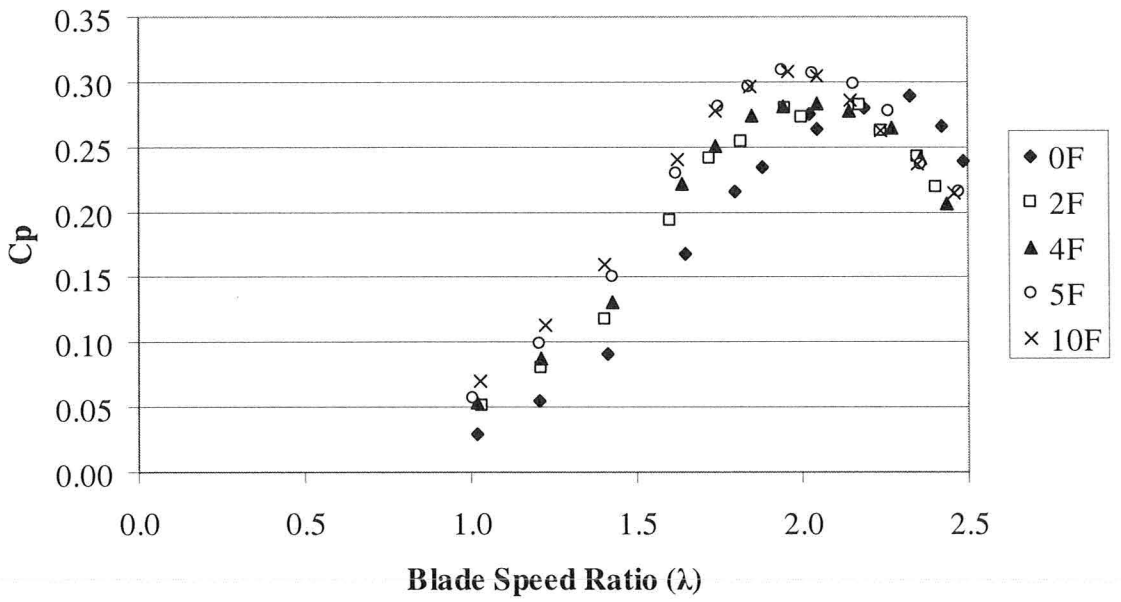

Figure 4-4: Power coefficient curves for canted blades showing the effect of fences. Wind speed is 8 m/s and pitch is β = -3.5° for all cases.

The impact of fences on power performance was even more pronounced at 6m/s as illustrated in Figure 4-5. Peak power output increased 20% from C_{Pmax} = 0.21 without fences to C_{Pmax} = 0.25 with five inboard fences while the optimal blade speed ratio changed similarly to the 8m/s tests. The reduction in the peak power blade speed ratio can again be attributed to the fences impeding spanwise flow along the canted blades. Restricting spanwise flow was likely also responsible for part of the power gain at 6m/s,

with an increase in effective Reynolds number accounting for the other part of the power increase.

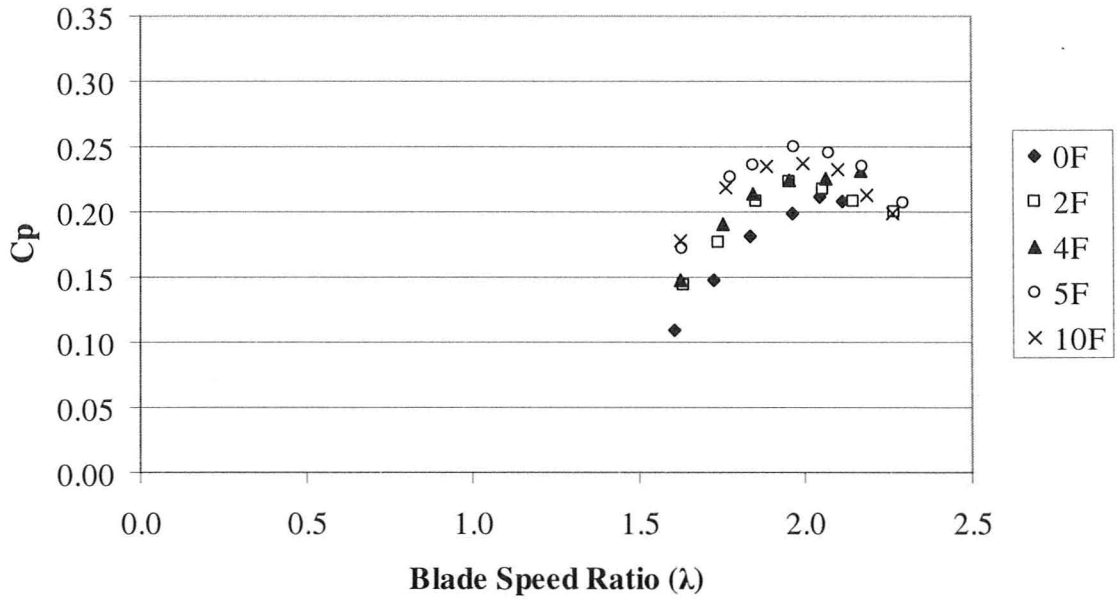

Figure 4-5: Power coefficient curves for canted blades showing the effect of fences. Wind speed is 6 m/s and pitch is β = -3.5° for all cases.

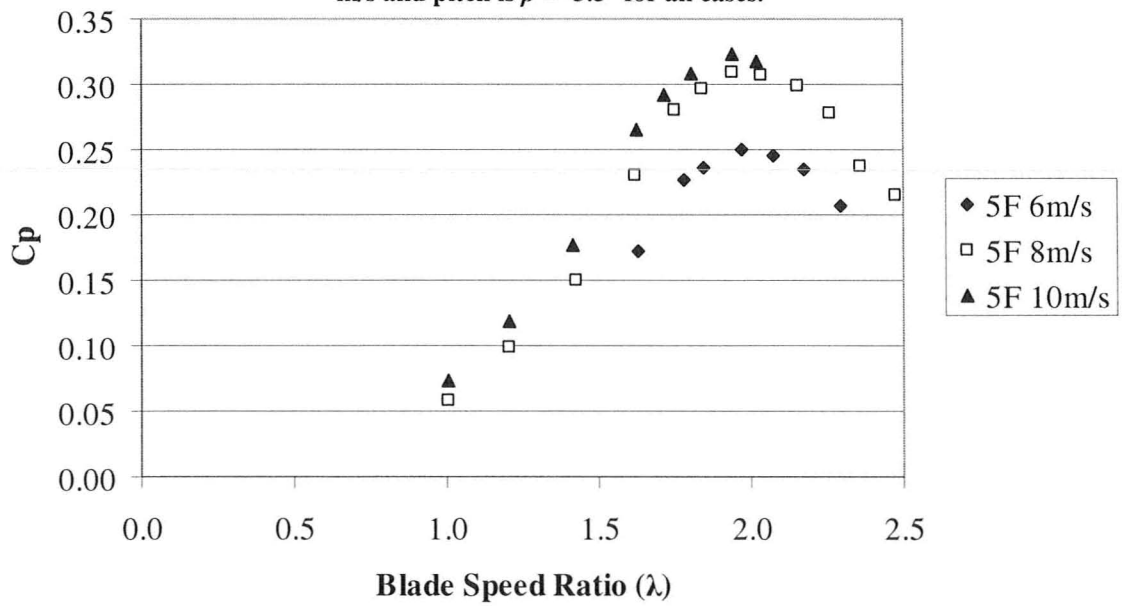

Figure 4-6: Power coefficient curves for canted blades with five fences showing the effect of wind speed (Reynolds number). Pitch is β = -3.5° for all cases.

Figure 4-6 shows an additional test of canted blades with five fences at 10 m/s wind speed along with the 8 m/s and 6 m/s wind speed five fences tests. The peak power coefficient of CP_{max} = 0.32 at λ = 1.93 for 10 m/s wind speed matches the highest observed power coefficient by Fiedler (2009) with straight blades and shows very little change in the power performance from canted blades at 8 m/s with fences.

A further test was performed with five inboard fences installed on the straight blades to identify any performance decreases associated with fences due to increased drag. Five fences were used for comparability since five fences gave the best power performance on canted blades. Figure 4-7 illustrates that at various wind speeds fences have no obvious impact on the optimal blade speed ratio or power coefficient of the straight blades. These results suggest that the fences themselves likely have little drag penalty when applied on canted blades.

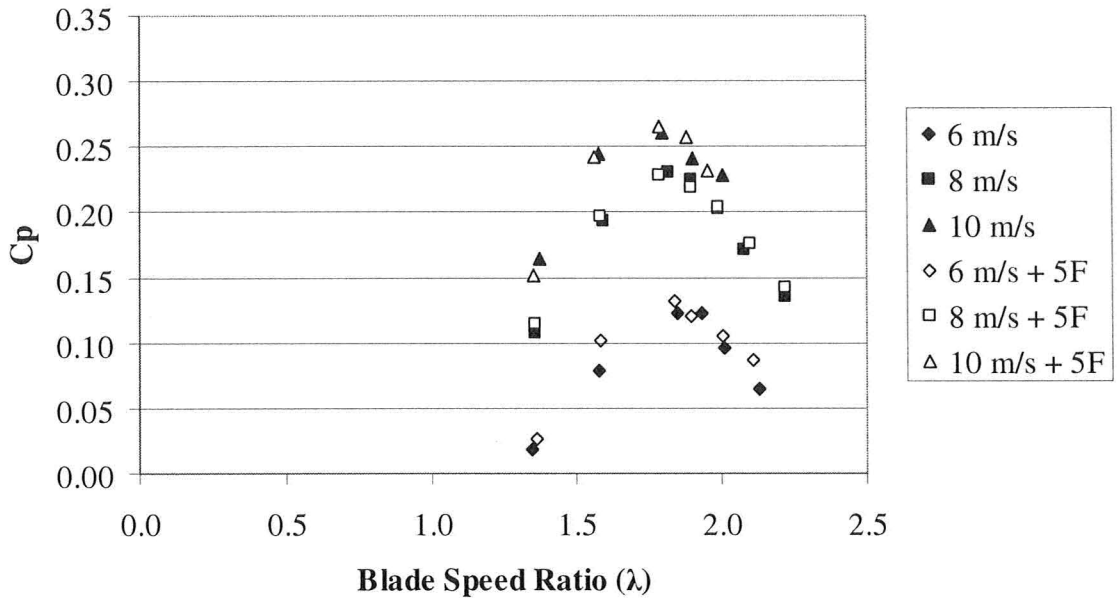

Figure 4-7: Power coefficient curves for the straight blades showing the effect of blade fences. Pitch is β = -3.5° for all cases.

4.2 Separation/Tufts of Straight and Canted Blade

As stated in Section 3.7, the initial investigation of separation behaviour on straight blades using tufts was performed by Fiedler (2009), where the amount of separation was binned into categories of no reversed flow, reversed flow at just the trailing (or leading) edge, reversed flow over half the chord and fully reversed flow (reversed flow over the majority of the chord). These flow patterns are shown in Figure 4-8. Fiedler's (2009) analysis focused on the azimuthal positions of initial separation and final reattachment as well as the duration of fully reversed flow, with comparisons between different blade speed ratios and preset pitches.

The separation behaviour of the straight blades is being presented here to give a context in which the separation behaviour of canted blades can be assessed and

compared. Further analysis was also performed on Fiedler's (2009) straight blade video footage but no new testing was performed. The flow reversal data is presented in two formats. First, a contour plot is presented for a base case at a given blade speed ratio, where colour intensity reflects the degree of reversed flow and shows the time evolution and location of reversed flow on the blade. Secondly, to compare data for other pitches and blade speed ratios in a concise manner, three-dimensional scatter plots are used to show the percentage of reversed flow at different blade speed ratios and azimuthal angles. In the scatter plots, the data point markers indicate angles where the video was analysed with the size of the markers roughly proportional to the magnitude of the error. For all plots, the error was about +/-5% for the separation fraction, +/-2° for azimuthal position and +/-0.05 for blade speed ratio. The power coefficient is plotted on the left of the scatter plots so that power performance can be related to the flow behaviour on the inner blade surface.

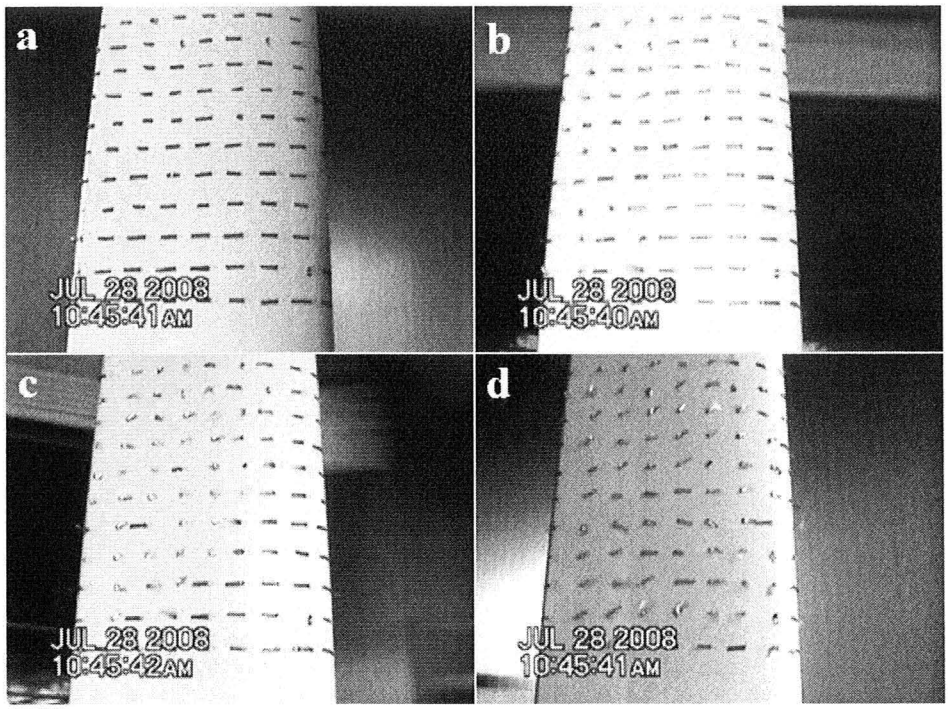

Figure 4-8: Flow patterns on the straight blade showing (a) no reversed flow, (b) trailing edge reversed flow, (c) reversed flow over the rear half chord and (d) reversed flow over the entire blade (Fiedler, 2009).

4.2.1 Separation Behaviour of Straight Blades

Figure 4-9 shows the development of reversed flow on a straight blade at $\beta = 0°$ and $\lambda = 1.6$. Reversed flow started to appear on the blade at $\theta = 60°$ between approximately 90% and 70% chord. The reversed flow progressed rearward to the trailing edge and forward on the blade to occur over almost the entire blade by $\theta = 160°$. Reattachment of the flow occurred rapidly from the trailing edge at $\theta \approx 200°$ to the leading edge so that no reversed flow was seen by $\theta = 230°$. No flow reversal was seen on the remainder of the downwind pass of the blade.

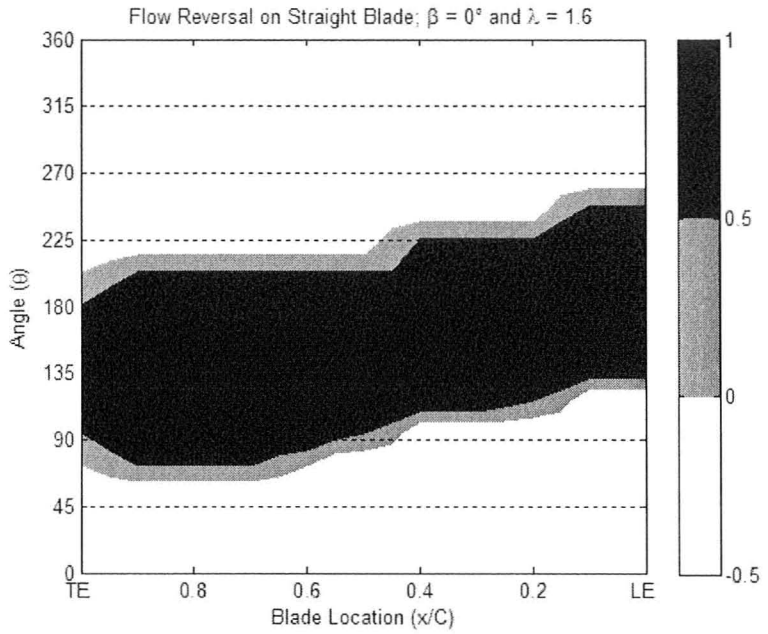

Figure 4-9: Development of reversed flow on a straight blade at $\beta = 0°$ and $\lambda = 1.6$.

It is significant that reversed flow was seen at $\theta = 180°$, where the nominal flow angle of attack is $\alpha = 0°$, and past $\theta = 180°$, where the inner blade surface is the pressure side on the blade. This agrees with previous flow visualization and CFD results that show the formation of a vortex on the inner suction surface of the blade before $\theta = 90°$, its shedding and its continued presence near the blade past $\theta = 180°$, for lower solidity blades at higher blade speed ratios (Ferreira, 2007) and similar solidity turbines at similar blade speed ratios (McLaren et al., 2009, Fiedler, 2009). Specifically, examination of the vorticity field on the blade surface presented by Ferreira et al. (2009) suggests that at $\theta = 90°$ reversed flow was present over the rear 85% of the chord, with reversed flow present at the trailing edge through to and possibly beyond $\theta = 110°$. At $\theta = 121°$, reversed flow was seen from about 30% chord to 90% chord, while at $\theta = 218°$ it appeared as though all but the trailing edge was experiencing reversed flow. There is general agreement in the

reversed flow patterns, where the differences can be explained by the lower solidity, σ = 0.125, higher blade speed ratio, λ = 2, and lower Reynolds number, Re=50,000, of the Ferreira et al. (2009) PIV data.

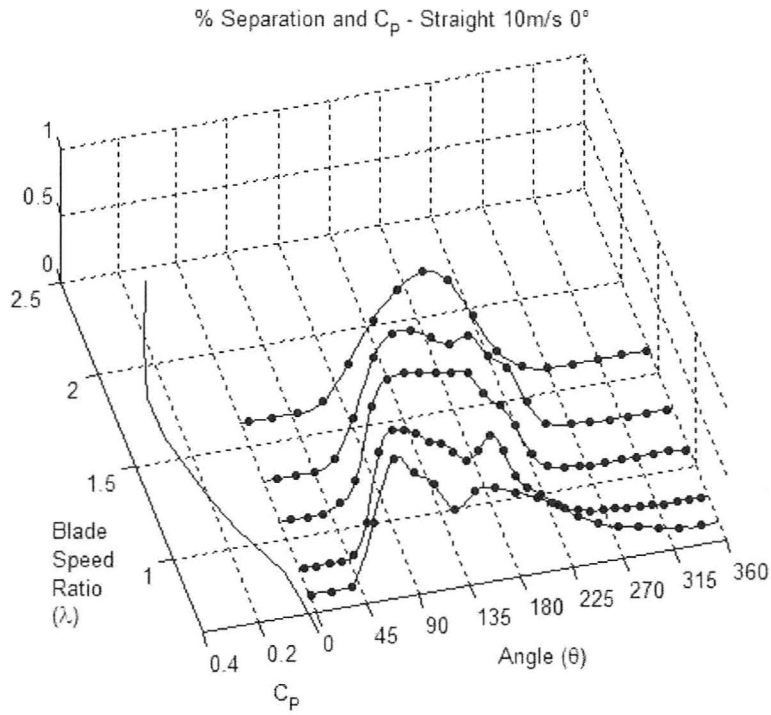

Figure 4-10: Flow separation curves for straight blades at β = 0° and a number of blade speed ratios.

Additional flow separation curves for straight blades at different blade speed ratios are shown for β = 0° in Figure 4-10. As the blade speed ratio decreased, reversed flow appeared earlier in the blade rotation, as early as θ = 45° for blade speed ratios of λ = 1.1 and less, and the progression to almost fully separated flow over the entire blade also occurred more rapidly. These changes are related to the increased angles of attack occurring at reduced blade speed ratios. For blade speed ratios below λ = 1, there was a pronounced interval of mid-chord reattachment at approximately θ = 150° that led to a reduction in reversed flow fraction. The subsequent reattachment after θ = 180°

progressed slowly from the trailing edge to leading edge, so the decrease in reversed flow fraction was more gradual than that at higher blade speed ratios. A further decrease in blade speed ratio to $\lambda = 0.7$ produced a larger reattachment at about $\theta = 140°$, and an even more gradual return to fully attached flow, which only occurred at about $\theta = 300°$. This reversed flow on the downwind pass of the blade is almost certainly due to the interaction of the blade with previously shed vortices as seen by Brouchier et al. [20], Fujisawa and Shibuya (2009) and McLaren et al. (2009) while the brief mid-chord reattachment is likely the result of a short-lived counter rotating vortex as seen in CFD simulations by McLaren et al. (2009).

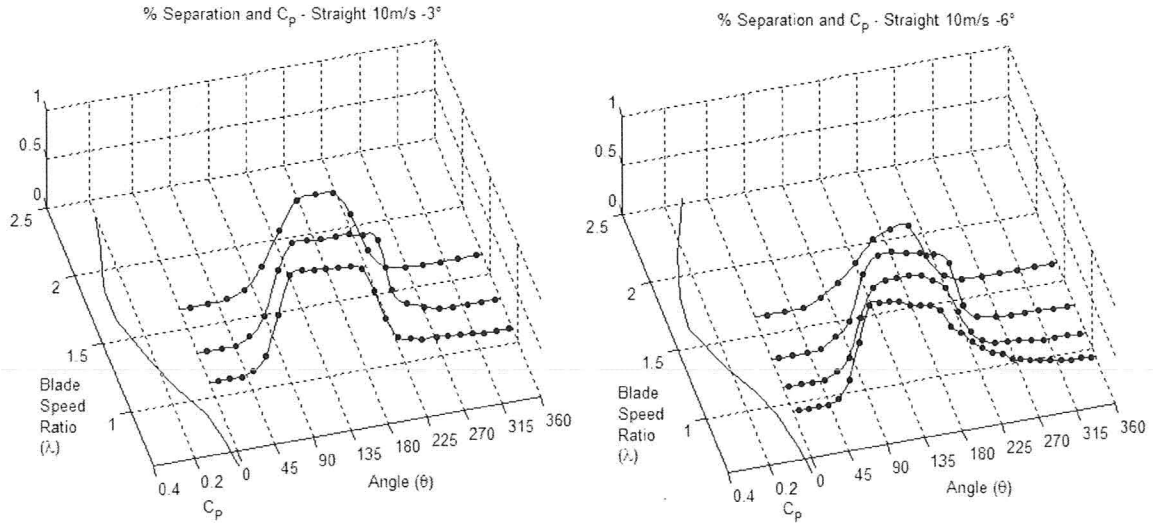

Figure 4-11: Flow separation curves for straight blades at $\beta = -3°$ and $\beta = -6°$ for a number of blade speed ratios.

Slight differences in the tuft patterns were seen when the blade was pitched toe-out, where peak power at a blade speed ratio of $\lambda = 1.6$ was seen to increase. For $\beta = -3°$, the flow reversal pattern seemed to be almost the same as at $\beta = 0°$ pitch. For $\beta = -6°$, the initial flow separation was seen at about 75% chord, and the size of the separation region

progressed more slowly to its maximum of only about 65% of the chord, at which point the flow at both the leading and trailing edges was attached. The reduced separation matches the simple model of toe-out pitch reducing the angle of attack on the upwind pass, although the azimuthal location of initial flow reversal remained essentially unchanged. At lower blade speed ratios of $\lambda = 1.3$ and $\lambda = 1.1$, there was again a distinct delay in the progression of flow reversal with increasing toe-out pitch. For an even lower blade speed ratio of $\lambda = 0.94$, the $\beta = -6°$ pitch case displayed momentary mid-chord reattachment at about $\theta = 130°$, similar to the more prolonged reattachment seen for $\beta = 0°$ pitch at very low blade speed ratios. The eventual reattachment was prolonged, much like the low blade speed ratios $\beta = 0°$ pitch cases.

4.2.2 Separation Behaviour of Canted Blades

The field of view on the canted blade is 500 mm below the turbine center (the same as for the straight blade). At this location on the canted blade, the radius is 10% less than at the strut where the blade speed ratio is reported, so the blade is actually traveling slower than the strut. For consistency with the power performance measurements, the blade speed ratio is reported with reference to the strut, however, the tufts are traveling slower. For example, at peak power with no fences, $\lambda = 2.15$, the tufts have a real blade speed ratio of $\lambda = 1.93$, which is closer to the straight blade speed.

The progression of flow reversal on a canted blade – $\beta = -1.5°$ and $\lambda = 2.15$ – is shown in Figure 4-12 and is noticeably different than the pattern on the straight blade. Separation appeared at $\theta = 75°$, started at the trailing edge and progressed forward on the

blade reaching about 50% chord around θ = 120°. Reattachment then occurred from both the trailing edge and the furthest forward extent of the separated region, and the flow was fully reattached by θ = 180°, with the last reversed flow seen around 80% chord. This behaviour is in contrast with the straight blades at their optimal blade speed ratio, where separation first occurred at θ = 60° and the separated flow extended well into the downwind pass (θ > 180°). Most of this behaviour is likely due to the higher peak power blade speed ratio of $\lambda = 2.15$ for the canted blades than for the straight blades at $\lambda = 1.6$, since at a higher blade speed ratio the angles of attack would be smaller and result in less separated flow.

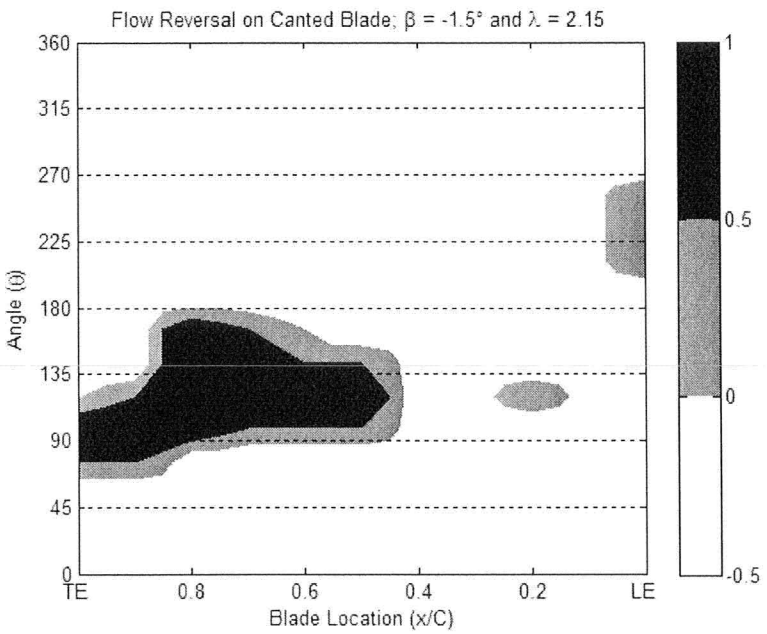

Figure 4-12: Development of reversed flow on a canted blade at β = -1.5° and λ = 2.15.

Figure 4-13 shows separation fraction curves for canted blades at β = -1.5° and a number of blade speed ratios. The flow patterns on canted blades at blade speed ratios from $\lambda = 1.6$ to $\lambda = 2$ were similar (in terms of azimuthal position of reversed flow) to

those at λ = 2.2 except that the reversed flow region extended farther forward on the blade to reach the leading edge resulting in higher separation fractions. Reattachment began at the trailing edge around θ = 150° as the separated region was still spreading towards the leading edge. Shortly after the reversed flow region reached the leading edge, reattachment progressed rearward from the leading edge for the λ = 1.9 case. The maximum separated flow fraction reached approximately 70% of the chord at a blade speed ratio of λ = 1.6. At this blade speed ratio and a pitch of β = 0°, the straight blades were at peak power and experienced a maximum separation fraction of 90%. At λ = 1.6, flow reversal was seen on the canted blades into and during the downwind pass, θ > 180°, but only a small amount and only at the leading edge.

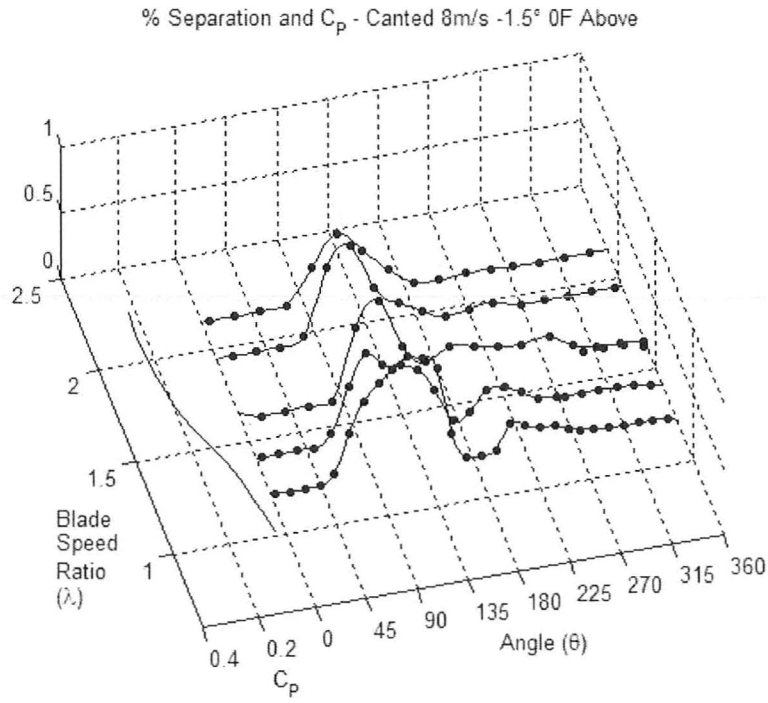

Figure 4-13: Flow separation curves for canted blades at β = -1.5° for a number of blade speed ratios.

At lower blade speed ratios of λ = 1.4 and λ = 1.2, flow separation was seen substantially earlier on the upwind pass, similar to that seen on the straight blades. However, the flow was fully reattached before θ = 180°. A separation region then grew from and retreated back to the leading edge during the downwind pass, similar to what was seen at λ = 1.6, except that at these blade speed ratios it was distinct from the initial trailing edge separation due to the fully reattached flow by θ = 180°.

It consequently appears that the initiation of separation on the canted blades is similar to that on the straight blades, however, the reversed flow associated with the continued interaction of the shed vortices is less on the canted blades. It is expected that vortex generation, shedding and subsequent interaction would be disrupted to some extent by the sweep as well as θ, solidity and blade speed ratio variations with height of the canted blades. The recovery from reversed flow at earlier angles is also similar to the phenomena observed by St. Hilaire et al. (1979) in testing oscillating unswept and Λ = 30° swept NACA 0012 airfoils. At low frequencies of oscillation, sweep reduced the severity of dynamic stall by reducing the magnitude of sudden changes in lift and pressure drag, an effect which diminished at higher frequencies. Therefore, it appears that canting the blades favourably altered the flow behaviour to facilitate earlier recovery from flow separation as compared to the straight blades. Furthermore, the second separation region seen at the leading edge appears to be interaction with a vortex formed on the same blade during the upwind pass. At blade speed ratios below approximately λ = 1.6 for β = -1.5° pitch, the vortex is completely shed resulting in full separation recovery, followed by impingement around θ = 200°. At a blade speed ratio of λ = 1.6,

the vortex is not fully shed and travels near the leading edge, while at blade speed ratios of $\lambda \geq 1.9$, the vortex is shed at mid-chord and the blade travels sufficiently faster than the convection speed of the vortex so no interaction occurs. For $\lambda < 1.9$, the leading edge vortex interaction was brief and appeared to merge with the reversed flow associated with the leading edge stagnation point.

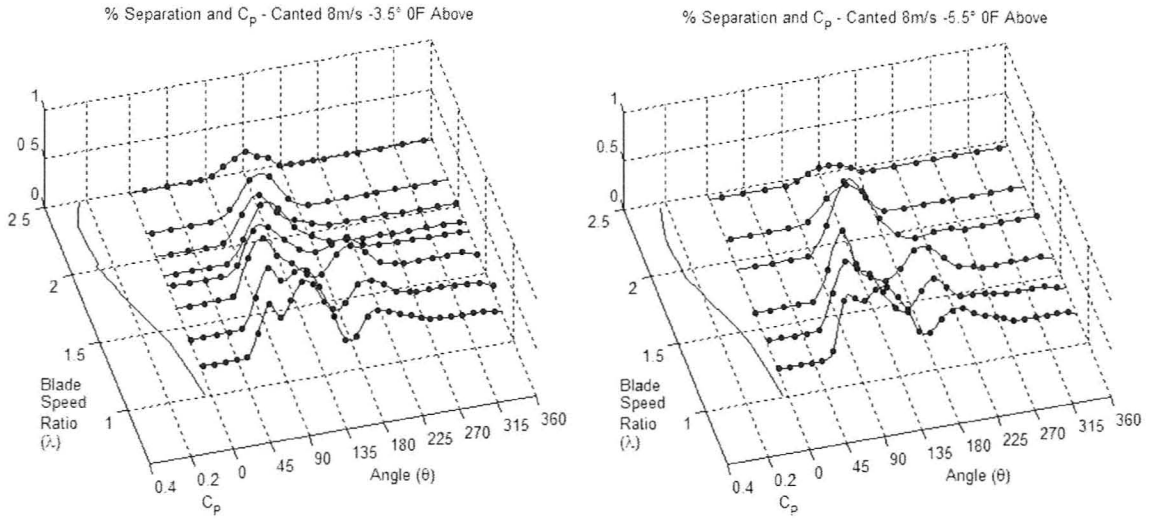

Figure 4-14: Flow separation curves for canted blades at β = -3.5° and β = -5.5° for a number of blade speed ratios.

The changes in flow separation with increasing toe-out pitch were small as shown in Figure 4-14. Table 4-1 summarizes the more significant changes. More negative pitch resulted in delayed initial separation and reduced maximum separation, consistent with observations on straight blades and the concept of more negative pitch reducing the angle of attack on the upwind pass. Higher blade speed ratios had similar effects. No downwind flow reversal was observed.

Table 4-1: Summary of key observations for reversed flow on canted blades

β	λ	Init. Sep. (θ)	Max. Sep. $\theta < 180°$	Max. Sep. $\theta > 180°$
-1.5°	2.15	75°	50%	0%
-3.5°	2.15	90°	40%	0%
-5.5°	2.15	100°	35%	0%
-3.5°	2.5	95°	20%	0%
-5.5°	2.5	105°	15%	0%

For β = -3.5° and β = -5.5°, like the β = -1.5° pitch case, flow reversal was only seen on the downwind pass for $\lambda < 1.9$. The downwind flow reversal was again limited to the leading edge and distinct from the upwind flow reversal. The most interesting feature of the downwind flow reversal was its increased extent with more negative pitch, up to 35% chord for β = -3.5° and 40% chord for β = -5.5°. At β = -1.5° the maximum extent was only 30%. The *change* in the extent of leading edge separation is consistent with the movement of a pressure side stagnation point that can be explained by non-vortex flow. As the pitch becomes more negative, the angle of attack increases on the downwind pass. Decreasing the blade speed ratio also increases the downwind pass angle of attack, not just by changing the rotational speed, but also by reducing the power extraction efficiency on the upwind pass, allowing higher wind speeds on the downwind pass. The large extent of separation, up to 40% of the chord on these moderately thin airfoils, suggests that blade-vortex interactions were still present in conjunction with the pressure side stagnation point.

4.2.3 Separation Behaviour of Canted Blades with Fences

The power performance increases resulting from the installation of fences on canted blades were accompanied by changes in the flow behaviour as shown in Figure 4-

15 for the case of β = -3.5° with five inboard fences. The discontinuities in these separation plots were the result of excessive light from the opening of the tunnel causing the video at those angles to be too washed out for analysis. There is a substantial decrease in the amount of separation with fences installed on the canted blades. As with no fences, flow separation does not occur past θ = 180° except for the same leading edge separation at low blade speed ratios. Downwind separation is only visible for $\lambda < 1.6$, which is lower than for the tests performed on canted blades without fences.

The flow patterns above and below the fences, corresponding to swept forward and swept aft, were different for λ = 1.9. Above the fence, the maximum flow reversal fraction was 50% as compared to only 10% below the fences. Reversed flow was concentrated in the upper rear portion of the tuft array above the fences with no reversed flow forward of 40% chord, except for a small patch of about four tufts near 30% chord immediately above the fences. This behaviour was different than below the fence where there was only a small band of separated tufts at the lower edge of the tuft array that moved from the trailing edge only as far forward as 50% chord. The flow behaviour above the fence was therefore much closer to what was observed without the fences, suggesting that it may be possible to modify the flow on the canted blade further with additional fences. As evidenced by the significantly reduced flow separation below the fence, fences could be an effective means of controlling the amount of dynamic stall on a canted blade thereby limiting aerodynamic load fluctuations to lower levels. If effective at reducing vibration, this dynamic stall control method would have to be balanced against the drag penalty from additional fences.

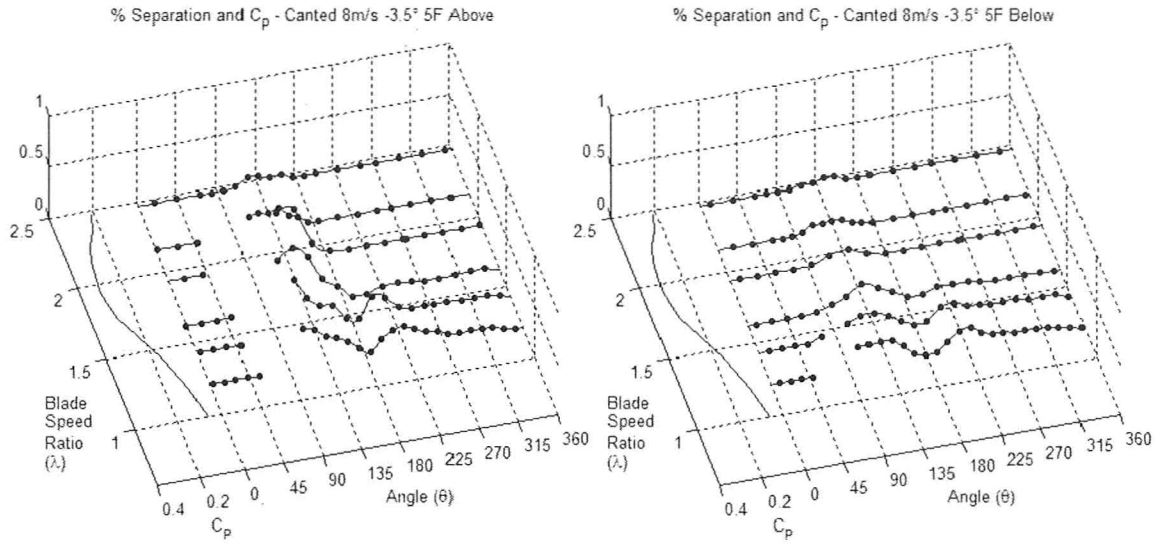

Figure 4-15: Flow separation curves for canted blades at β = -1.5° with five inboard fences for a number of blade speed ratios.

Reduced flow reversal was observed at all blade speed ratios with fences installed on the canted blades as compared to without fences and was especially prominent below the fence. Increasing the blade speed ratio had the same effect of delaying initial flow separation and reducing the maximum amount of separation as seen for straight blades and canted blades without fences. Decreasing the blade speed ratio produced the opposite effects. Therefore, canted blades with fences operate similarly to canted blades without fences and to straight blades. Furthermore, the fences appear to restrict spanwise flow and limit the boundary layer thickness on canted blades which allows the blades to operate at higher angles of attack with reduced dynamic stall effects.

4.3 Solidity and Pitch of Straight Blades

Additional testing was performed on the set of straight blades used for the tuft flow visualization analysis. The blades were tested for power performance over a range

of pitches and in a two-blade configuration. Testing of the three-bladed variant was the basis of Fiedler's (2009) work. The purpose of these two-bladed tests was to add to the understanding of the blade speed ratio versus solidity relationship and to examine how optimal pitch may change with solidity (and optimal blade speed ratio) given the differences in optimal pitch observed by Fiedler (2009) and by Klimas and Worstell (1981) for their different solidity turbines.

Figure 4-16 shows the new data added to the previously discussed solidity-blade speed ratio trends. The more recent data shows that the optimum blade speed ratio is lower at a given solidity than previously suggested by the NACA 0015 trend for $\beta = 2.5°$, which can be explained by examining Fiedler's (2009) pitch results.

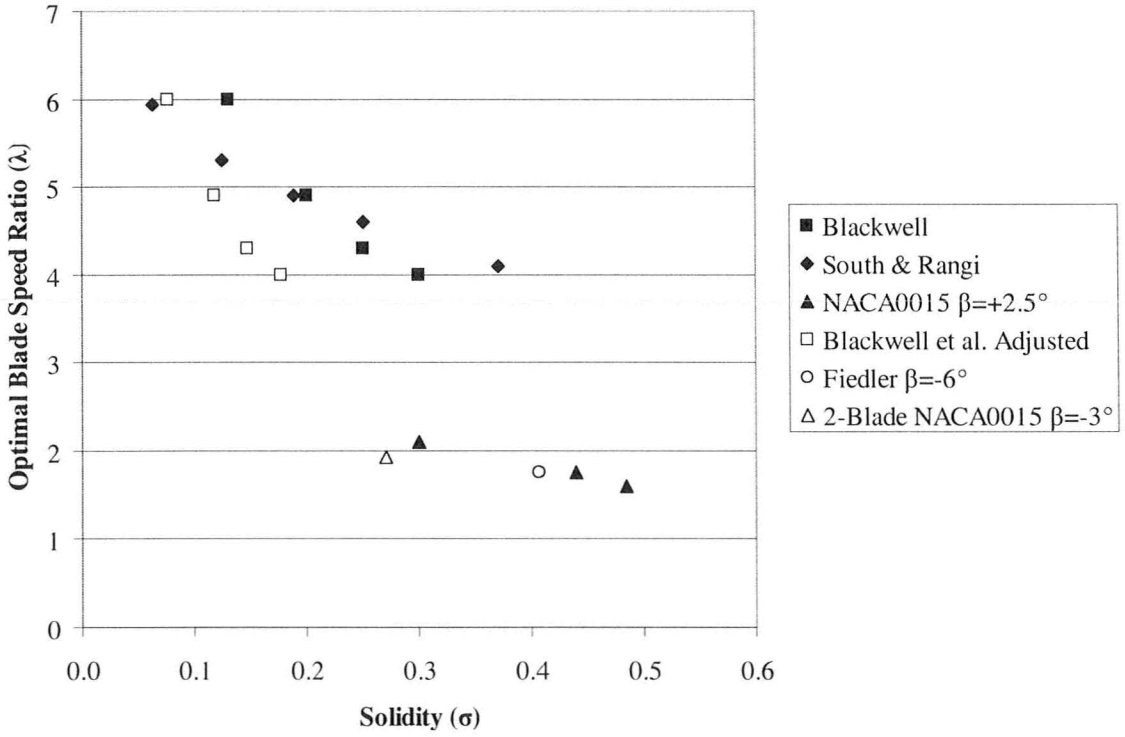

Figure 4-16: Optimal blade speed ratios for a number of solidities for vertical axis turbines.

Figure 4-17 is reproduced from Fiedler's (2009) three-bladed pitch tests. It shows that at β = +3° and β = -9° the peak blade speed is higher than for the cases where performance was higher (β = 0°, β = -3°, β = -6°). As a result of the effective pitch for the unpublished solidity variation tests, the peak blade speed ratio appeared higher because it was not reported at the best pitch. Figure 4-18 shows results from the two-bladed tests. No test was performed at β = +3° so it is uncertain to how the peak blade speed ratio changed for toe-in pitch at this solidity. The β = -6° and β = -9° tests show that the peak blade speed ratio is higher at pitches beyond the preset pitch with the best power performance, β = -6°, which is consistent with the three-bladed findings.

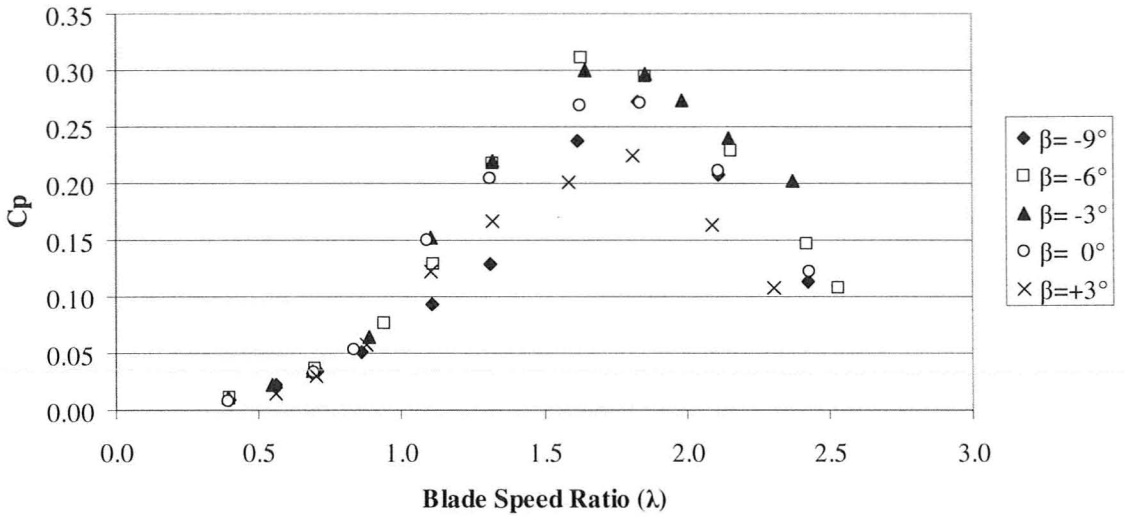

Figure 4-17: Power coefficient data for Fiedler's (2009) three-bladed pitch tests of straight blades at 10 m/s wind speed. Solidity is σ = 0.41.

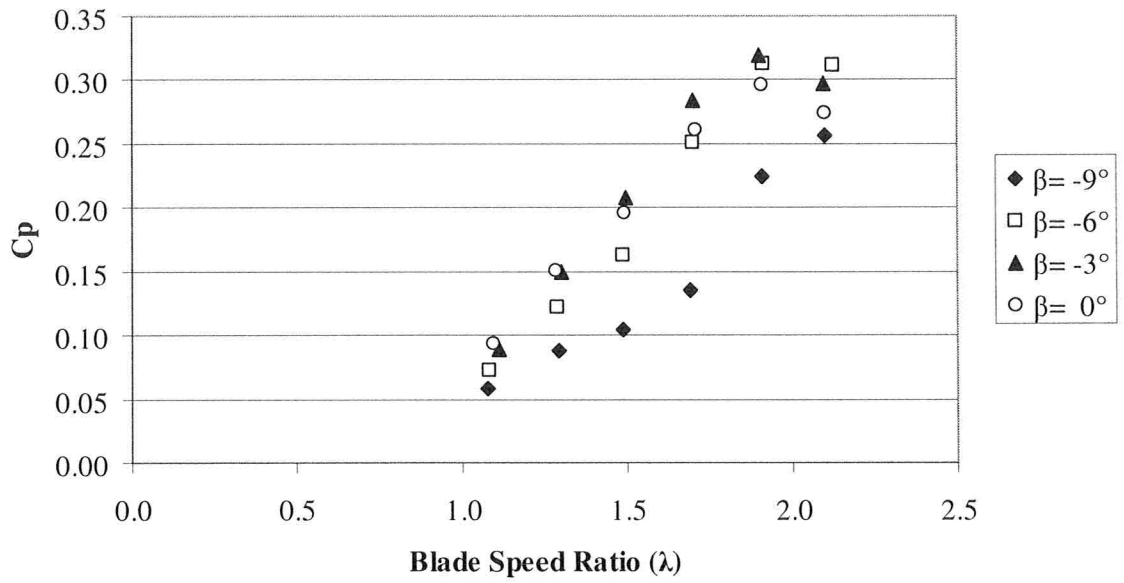

Figure 4-18: Power coefficient data for two-bladed pitch tests of straight blades at 10 m/s wind speed. Solidity is $\sigma = 0.27$.

A relationship between optimal pitch and blade speed ratio and solidity can also be extracted from Figures 4-17 and 4-18. Figure 4-19 shows the results of identifying C_{Pmax} on each of the power coefficient curves for the two- and three-bladed pitch tests as well as the canted blade tests. For the higher solidity, $\sigma = 0.41$, three-bladed tests the optimal pitch was close to $\beta = -6°$ while for the two-bladed tests, $\sigma = 0.27$ optimal pitch was close to $\beta = -3°$. Canted blades appear to be much more pitch sensitive than the straight blades. The data was also examined to show how optimal blade speed ratio changed with pitch, which showed that near optimal pitch, the peak power blade speed ratio reached a minimum.

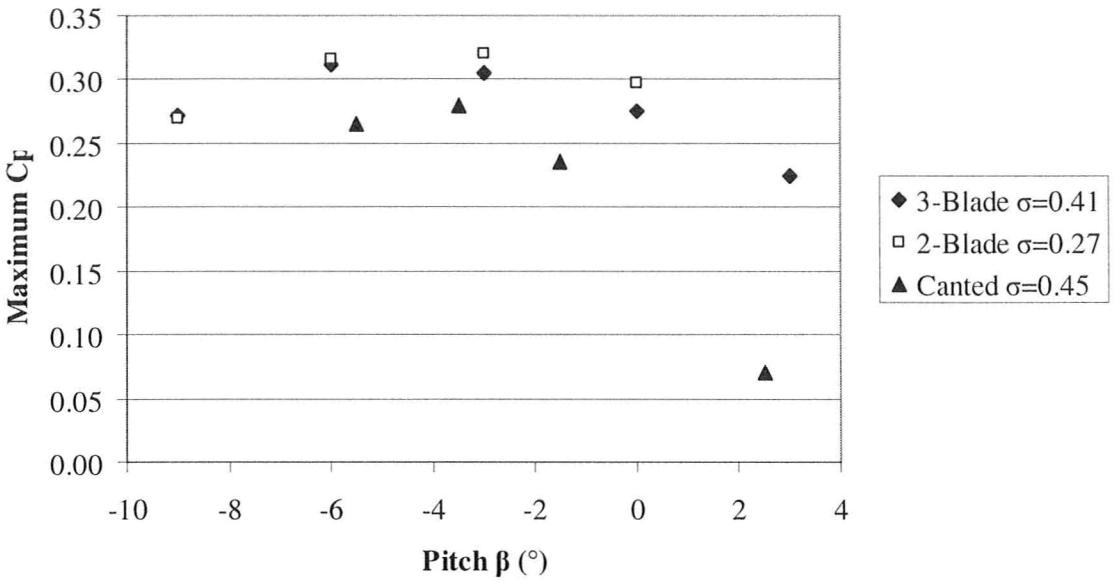

Figure 4-19: Relationship between pitch and the peak power coefficient achieved at the respective pitch for three straight blades, two straight blades and three canted blades.

The implications of pitch versus C_{Pmax} and pitch versus blade speed ratio are very important for canted blades due to their variable radius and variable local blade speed ratio. It is therefore likely that canted blades require a variable preset pitch along their length as compared to the constant preset local pitch used on the current blades. More specifically, canted blades should have less pitch (closer to $\beta = 0°$) near the tips where blade speed ratio is highest (solidity is lowest) and more negative pitch near the waist where the blade speed ratio is least as compared to a canted blade with constant pitch referenced at the strut. For example, since the best pitch for canted blade observed presently was $\beta = -3.5°$, the pitch at the tips and waist would be $\beta = -2.5°$ and $\beta = -4.5°$, respectively, although the exact values need to be determined from experiment or simulation. The need for variable pitch can explain the particular power performance sensitivity of canted blades to pitch changes as compared to straight blades. The blades

were likely only operating at the optimal pitch near the struts, whereas the tips and waist were probably operating off-peak, such that any incremental pitch change would increase the performance of one section of the blade at the expense of another section.. This type of situation could be identified by a relatively flat peak power region, which was the case observed with the canted blades.

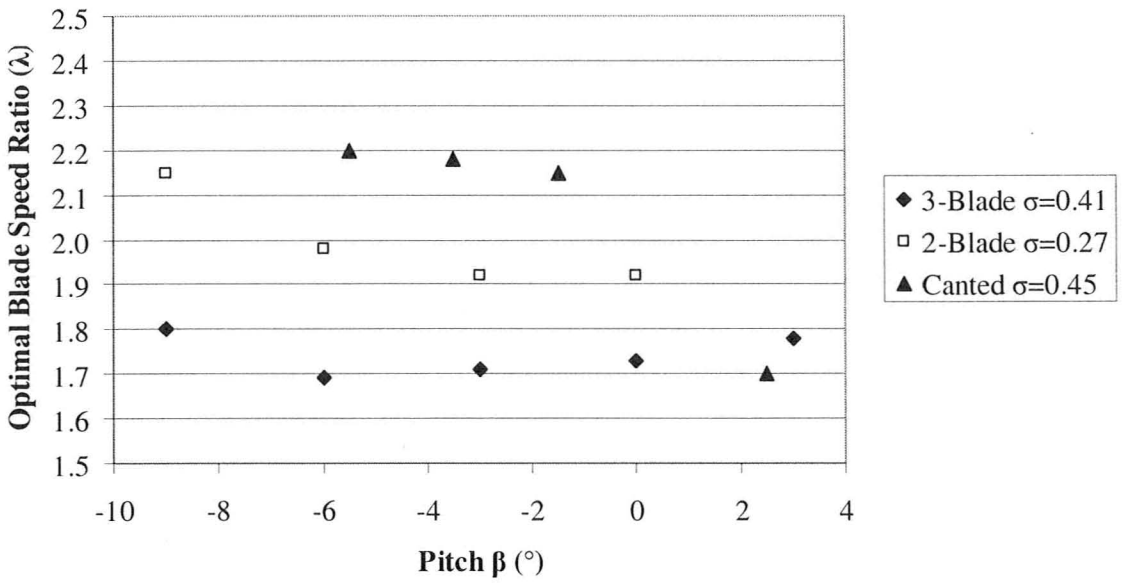

Figure 4-20: Relationship between pitch and optimal blade speed ratio at the respective pitch for three straight blades, two straight blades and three canted blades.

Figure 4-20 shows the effect of pitch on the optimal blade speed ratio. For the two straight blade cases, a certain pitch exists which results in a minimum optimum blade speed ratio. For the higher solidity three-blade case, this pitch was β = -6° and for the two-blade case this pitch was β = -3°, which suggests that the pitch affects the optimal blade speed ratio. It is interesting that these pitches were very close to the best overall peak power performance observed for their respective blade configuration. These results may be explained with Paraschivoiu's (2002) numerical decomposition of the overall

power coefficient curve for a vertical axis turbine into separate curves for the upwind and downwind passes. Parashivoiu (2002) showed that the upwind pass generates significantly more power than the downwind pass and that the upwind pass has a blade speed ratio at its peak power coefficient. Therefore, for a given solidity, it is possible that the optimal pitch results in a substantially larger increase in power performance of the downwind pass as compared to the upwind pass which lowers the optimal blade speed ratio of the net power coefficient curve.

Canted blades did not exhibit the same trend of a minimum blade speed ratio at the optimal pitch, which is likely the result of non-optimal pitch along the length of the present canted blades.

4.4 Excitation Response of Straight and Canted Blades

This section presents the excitation response of the turbine with canted blades and straight blades (420mm chord) installed at β = -3.5° pitch by measuring the response of two accelerometers located at the top of the shaft. The excitation response does not measure the loads producing excitation (blade loads), rather it measures the vibration of at the top of the shaft which is affected by a number of factors including the excitation loads and the proximity of the operating speed (and multiples of the operating speed) to the natural frequencies of the turbine. McLaren et al. (2010) used a set of struts instrumented with strain gauges to measure loads on straight blades directly, however, it was not possible to measure the canted blade loads the same way because of additional bending moments caused by the offset of the struts with canted blades. Accelerometers

measured the excitation response in the flow direction (stream-wise), and transverse to the flow direction (cross-stream). Measurements presented here are in the stream-wise direction, which were typically about 10% to 15% lower than for the cross-stream direction and show the same trends. The cross-stream excitation response plots and additional stream-wise plots are presented in Appendix B.

Figure 4-21 shows the stream-wise power spectral density excitation responses of canted blades and straight blades at 8m/s wind speed as a function of frequency and turbine rotational frequency, ω. Peaks at the rotational frequency (1N) show excitation response produced by mass unbalance of the turbine. Peaks at 3N, the blade pass frequency, represent aerodynamic excitation, by far the most significant source of excitation. Also shown in Figure 4-21 is the lowest turbine natural frequency, which corresponds to the turbine shaft "whirl" mode (essentially three-dimensional bending of the shaft near the base of the generator). For canted blades the whirl frequency was approximately 7.2 Hz and for straight blades was approximately 6.8 Hz, with the difference due to the different mass and stiffness of the two configurations. There is evidence (McLaren et al., 2010) that, for the straight blade case, the whirl mode frequency splits into two separate frequencies and is not constant as the turbine RPM increases. Higher modes, which include strut modes (McLaren et al. 2010) have been omitted from the figure. The optimal operating region of the turbine is shown as a band in the figure. Coincidence of the turbine natural frequency(ies) with a multiple of the turbine rotation frequency (particularly the 3N blade pass frequency) represents resonance, and the turbine rotation rate that produces this coincidence should be avoided.

Since the optimal turbine rotation rate is a function of wind speed, at some wind speed the optimal turbine RPM will be at the resonance conditions (in practice, at these wind speeds, the turbine is run at off-optimal RPM to avoid this resonance).

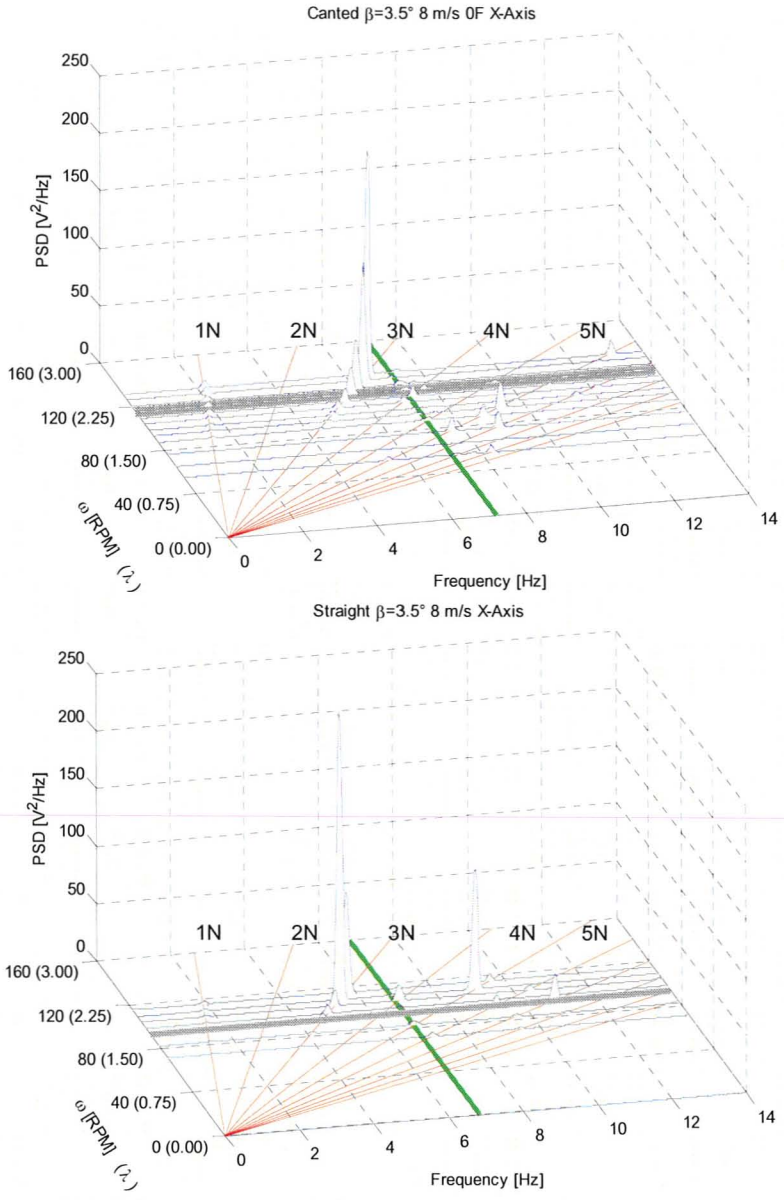

Figure 4-21: The stream-wise excitation response at 8 m/s wind speed and β = -3.5° of (a) a canted blade without fences and (b) a straight blades. The gray constant RPM band indicates the optimal operating range of blade speed ratios, and the green constant frequency (Hz) band indicates the turbine shaft whirl natural frequency. The red rays correspond to multiples (1N, 2N, 3N…) of the turbine rotational rate ω with respect to frequency in Hz

The excitation response occurs primarily at the blade pass frequency (3N) for both cases shown in Figure 4-21. The power spectral density is seen to increase as the natural frequency associated with the primary whirl mode was approached. The maximum power spectral density observed for straight blades was 250 V^2/Hz at 5.44 Hz (109 RPM, λ = 2.1) where the turbine was operating with a power coefficient of C_P = 0.18 and producing a net power of 450 W. The maximum power spectral density observed for canted blades was 195 V^2/Hz and occurred at a frequency of 6.6 Hz (131 RPM, λ = 2.5) where the turbine was operating with a power coefficient of C_P = 0.24 and producing a net power of 572 W. Neither blade type reached its respective nominal natural whirl frequency at this wind speed, although, for the straight blade case, the maximum turbine RPM appears to be past the resonance peak, while for the canted blades, the vibration is still increasing at the maximum RPM reached.

A direct comparison between straight blades and canted blades is not possible because they operate at different optimal blade speed ratios such that peak power does not occur at the same rotational frequency. At 8 m/s wind speed, the peak power of canted blades occurs at approximately 3N = 5.8 Hz, while the peak power of straight blades occurs around 3N = 4.7 Hz. Therefore, at peak power, the canted blades operated much closer to their whirl frequency. Furthermore, the nominal whirl frequencies of the canted blade turbine and straight blade turbine are different, 7.2 Hz and 6.8 Hz, respectively, which makes the comparison more challenging. The area of the turbine with canted blades installed, 8.16 m^2, is also less than the area when straight blades are installed, 8.61 m^2.

One way that the excitation response may be compared is though normalization of the data. Differences in the operating and natural frequencies can be minimized if multiple wind speeds can be compared. However, changing the wind speed also changes the power output. Therefore, the data can be normalized by the wind power to eliminate changes in power output related to wind speed and differences in blade planform area between straight blades and canted blades. Table 4-2 shows a number of cases of interest for comparison using the normalization procedure.

Table 4-2: Summary of the excitation response results for straight and canted blades and canted blades with fences

Blade	Wind Speed (m/s)	Fences (#)	Peak Power			Nat. Freq. (Hz)	3N / Nat. Freq.	C_P	Avg. Wind Power (W)	Pk. Net Power (W)
			λ	RPM	3N (Hz)					
Canted	8	0	2.18	115	5.8	7.2	0.80	0.28	2415	676
Canted	8	0	2.29	120	6.0	7.2	0.83	0.27	2415	657
Canted	8	5	1.94	104	5.2	7.2	0.72	0.30	2463	745
Canted	9	0	2.15	129	6.5	7.2	0.90	0.29	3657	1036
Canted	10	5	1.94	130	6.5	7.2	0.90	0.32	4945	1565
Straight	8	0	1.78	93	4.7	6.8	0.68	0.23	2584	597
Straight	10	0	1.78	116	5.8	6.8	0.85	0.27	5208	1350

To assess the accuracy of the normalization, two configurations that should have similar excitation responses should be compared first. By adding fences to the canted blades, the optimal (peak power) rotational frequency can be changed without appreciably affecting the aerodynamics, although some change does occur as shown with tuft flow visualization. The natural frequencies do not change by adding fences. Therefore, for comparison, the cases of canted blades at 9 m/s wind speed without fences and canted blades at 10 m/s with five fences are shown normalized by the wind power in Figure 4-22. Here, two-dimensional plots are shown to present the 3N aerodynamic

excitation more clearly. For these cases, the rotational frequencies at peak power are the same and so is the whirl natural frequency.

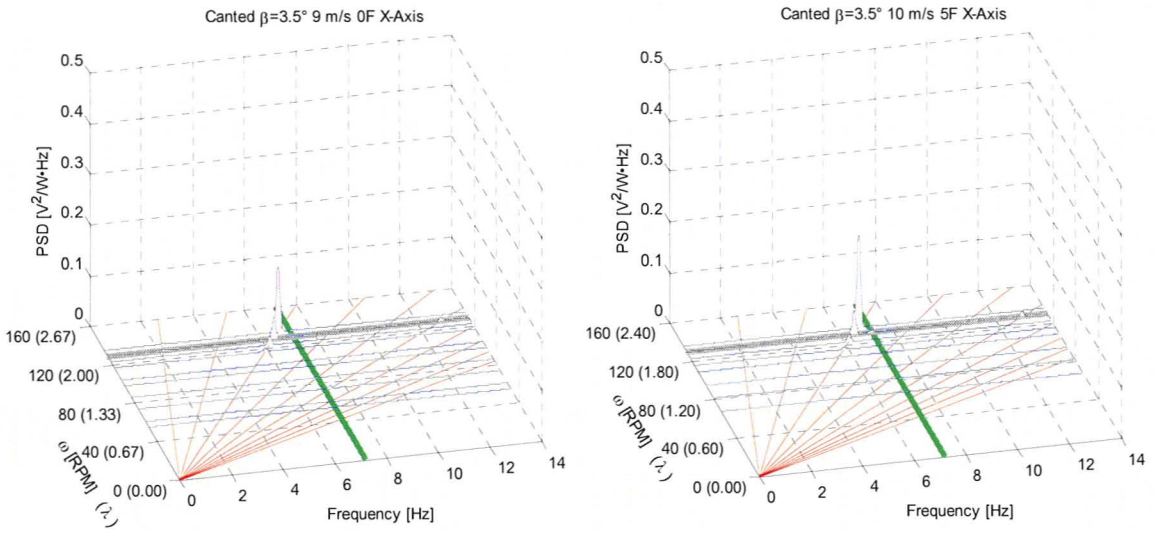

Figure 4-22: The normalized stream-wise excitation response at β = -3.5° for (a) canted blades without fences at 9 m/s wind speed and (b) canted blades with five inboard fences at 10 m/s wind speed.

At peak power, the normalized excitation response was 0.041 V^2/W•Hz for the without fences test at 9 m/s wind speed and at 10 m/s wind speed with five fences the normalized response was 0.047 V^2/W•Hz. The difference between the responses of the two tests is 13%. This is approximately equal to the 10% difference in power coefficient between the two cases, C_{Pmax} = 0.32 at 10 m/s with fences and C_{Pmax} = 0.29 for 9 m/s without fences. This makes sense considering that these peaks are aerodynamic (3N) excitations and fences impact the aerodynamic performance. It also suggests that, in the current configuration, fences do not affect the excitation response any more than they affect the power performance. It therefore appears that normalizing the data by the peak power output may be more appropriate when changes to the testing parameters or turbine affect the power output by modifying the aerodynamic behaviour.

Looking back to Table 4-2, the best comparison between canted blades and straight blades is 8 m/s for canted blades to 10 m/s straight blades because their rotational frequencies and power coefficients are nearly identical at peak power. The ratio of the aerodynamic excitation frequency (3N) to the natural whirl frequency (measured as 3N / Nat. Freq.) is also closest for these cases, 0.80 for canted blades and 0.85 for straight blades. This comparison is show in Figure 4-23.

The maximum response of canted blades is approximately 20% of the maximum response of the straight blades. A number of higher modes are also excited to a greater extent with the straight blades that with canted blades. At peak power, the normalized excitation response of the canted blades is 0.0095 V^2/W-Hz and for the straight blades is 0.022 V^2/W-Hz. It therefore appears that, within the limitations of the normalization, excitation response is less with canted blades.

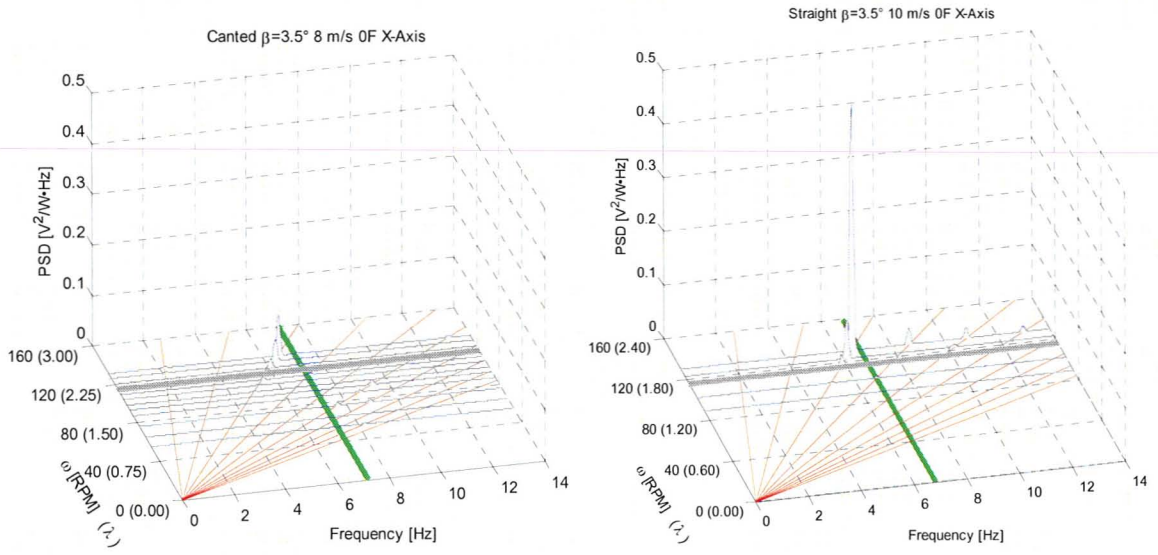

Figure 4-23: The normalized stream-wise excitation response at β = -3.5° for (a) a canted blade without fences at 8 m/s wind speed and (b) a straight blade at 10 m/s wind speed.

The ratio of the aerodynamic excitation frequency to the natural whirl frequency has a very significant impact on the excitation response. In the above comparison, the canted blades were operating at a lower ratio, 0.80 vs. 0.85, at peak power than the straight blades which biased the response of the canted blades to a lower value since they were farther from resonance. If the response of the canted blades is examined at a rotational frequency just above peak power, the frequency ratio is closer at 0.83 where the highest normalized response is 0.017 V^2/W-Hz. This is still less than for the straight blades, but is much closer, and illustrates how important the chosen operating point is for comparison.

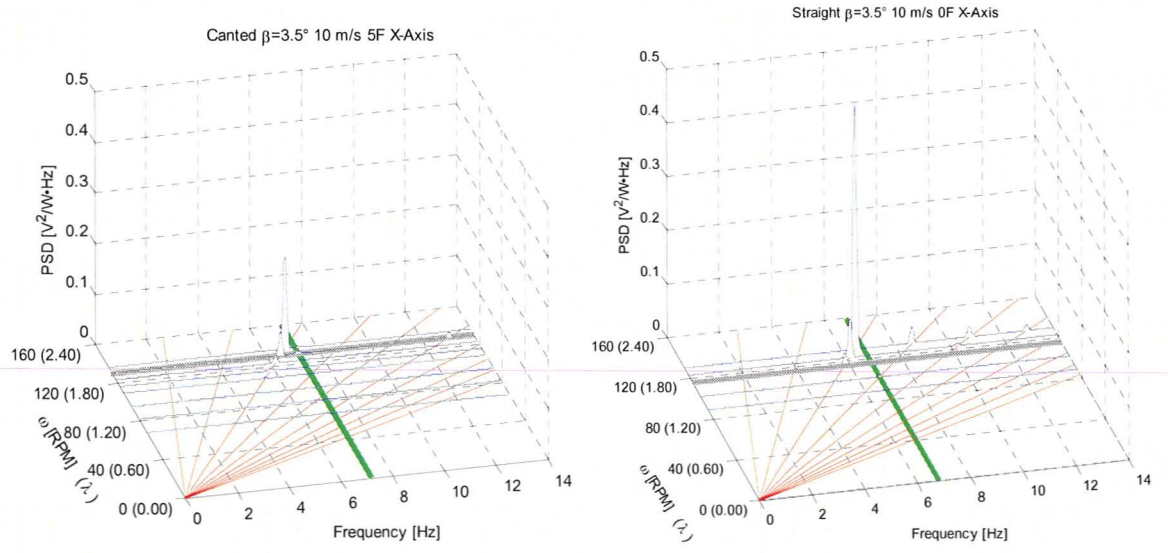

Figure 4-24: The normalized stream-wise excitation response at β = -3.5° and 10 m/s wind speed for (a) a canted blade with five inboard fences and (b) a straight blade.

The most interesting case is having both blade configurations operating at resonance at peak power, which could not be achieved in the present tests. The closest that was achieved was with straight blades at 10 m/s wind speed and canted blades with five fences at 10 m/s wind speed as show in Figure 4-24. At the highest observed

excitation responses, canted blades were operating at a frequency ratio of 0.94 with C_P = 0.31 and straight blades at a ratio of 0.95 with C_P = 0.23. The canted blade excitation response was less than 40% of the straight blade response, despite producing more aerodynamic power, 1570 W vs. 1260 W.

The excitation response results suggest that canted blades exhibit a lower excitation response than straight blades, although it is difficult to quantify the exact difference in excitation response due to the different natural frequencies, different optimal operating points and differences in power outputs. Any new set of canted blades built for testing should be designed to operate closer at peak power to the blade speed ratio of the straight blades used for comparison. Normalizing the excitation response data appears to work and allows comparisons to be made if the natural frequencies and operating points do not match exactly. This method would work best if tests are performed above the Reynolds number dependence limit. Careful selection of the wind speed can also be made so that, at peak power, the ratio of the aerodynamic excitation frequency to the natural frequency is identical for all configurations tested. The ideal case for comparison would be to operate both blade configurations at resonance although this would be difficult in practice.

CHAPTER 5: CONCLUSIONS AND RECOMMENDATIONS FOR FUTURE WORK

5.1 CONCLUSIONS

Performance testing and flow visualization of a vertical axis wind turbine was carried out in an open-air wind tunnel at the University of Waterloo Fire Research Facility. Straight and canted blades were tested using a prototype version of the small-scale H-Darrieus turbine.

Canted blades were tested at pitches of β = +2.5°, -1.5°, -3.5° and -5.5°. Measured power was highest at β = -3.5° where the optimal blade speed ratio was λ = 2.15 and was C_{Pmax} = 0.28 for 8m/s wind speed (Re = 5.5×10^5). The full set of performance curves suggest that the optimal pitch was very near β = -3.5° for this particular set of canted blades. Severe performance sensitivity was seen for the toe-in pitch case and overall this set of canted blades showed higher sensitivity overall to changes in preset pitch as compared to straight blades. It is therefore very important that canted blades have the correct preset pitch to ensure good power performance. The blade speed ratio at peak power appeared to increase slightly with increasing pitch. The optimal blade speed ratio of the canted blades was about 25% higher than equivalent straight blades despite nearly identical solidities.

A number of different wind speeds were tested at a pitch β = -3.5° pitch. Some Reynolds number effects appeared to still be present at 8m/s because the power

coefficient at 9m/s ($Re_c = 4.8x10^5$) was slightly higher at $C_{Pmax} = 0.29$ compared to $C_{Pmax} = 0.28$ at 8 m/s. The peak blade speed ratio did not change however. The change in power coefficient of $\Delta C_P = 0.01$ was much smaller than the change of $\Delta C_P = 0.03$ from 7m/s to 8m/s wind speed so the 8 m/s wind speed tests were considered to be at the threshold of the Reynolds number independence limit. Overall, the Reynolds number dependence of canted blades was in-line with trends observed for straight blades by Bravo et al. (2007) and Fiedler (2009).

Blade fences were tested on canted blades for their effect on power performance. Two inboard fences reduced the optimal blade speed ratio from $\lambda = 2.15$ to about $\lambda = 2.05$ with no noticeable power improvement, while five inboard fences further reduced the optimal blade speed ratio to $\lambda = 1.9$ and increased the power coefficient by 7% to $C_{Pmax} = 0.30$ at 8m/s wind speed. The addition of outboard fences (to already present inboard fences) did not noticeably change the power performance.

Flow visualization using tufts showed that canted blades experienced less flow reversal than the straight blades over the entire range of azimuthal angles, but especially during the downwind pass, where, at blade speed ratios above approximately $\lambda = 1.8$, no flow reversal was seen. At lower blade speed ratios, a second distinct separation region was observed during the downwind pass originating at the leading edge that was likely the result of a blade-vortex interaction. Increasing the amount of toe-out pitch delayed the onset of flow reversal to later azimuthal angles and reduced the maximum amount of observed flow separation during the upwind separation while increasing the extend of leading edge separation at low blade speed ratios during the downwind pass. With five

fences installed, flow reversal above the fence (swept forward) was reduced slightly while below the fence (swept aft) flow reversal was substantially reduced and mostly limited to the rear half of the chord. Fences also reduced the blade speed ratio at which the blade-vortex interaction could be seen on the downwind pass to below $\lambda = 1.6$.

Additional testing of two straight blades at a solidity of $\sigma = 0.27$ and at a number of pitches showed that the optimal pitch was less toe-out (closer to neutral) than what had been observed by Fiedler (2009) for his higher solidity case. The optimal blade speed ratio of the lower solidity configuration was higher. This has power performance optimization implications for canted blades where the solidity and blade speed ratio vary along the blade.

A direct comparison of the excitation response between canted blades and straight blades was not possible due to the differences in the natural frequencies, optimal operating speeds and to a lesser extent the rotor areas. Normalizing the results by the wind power allowed comparisons at different wind speeds so that the cases under consideration were operating at similar proximity to resonance. The data suggests that canted blades exhibit an excitation response of less than half the response of comparable straight blades while at the same time operating with a higher power coefficient although further testing is required to confirm this. However, it is not clear how much of this difference may be due to the sensitivity of the excitation response to proximity to resonance. Based on promising preliminary results, quantifying the difference in excitation response between canted blades and straight blades warrants further research.

5.2 Recommendations for Future Work

Optimizing the design of canted blades is more complicated than for straight blades as there are a number of additional parameters to consider including: the cant angle; the local solidity variation; and the pitch variation. These parameters are interrelated. The overall pitch, solidity and airfoil (thickness or camber) may also be examined. It is therefore recommended that a further series of systematic tests be performed with straight blades over a range of solidities and pitches to clearly identify the solidity versus blade speed ratio versus pitch relationship. The nature of the tests may be experimental or computational, where the importance of three dimensional simulations for power performance has been outlined by Howell et al. (2010). The simplest way to achieve different solidities is to use a combination of existing blades in two- and three-bladed configurations with struts and spacers or modified shorter struts. The same pitch adapters could be used, although a slightly finer $\Delta\beta = 2°$ pitch resolution would be preferred. Performing the experiments would provide an excellent database that simulations could be validated against. Once these relationships are fully quantified, a new set of canted blades could be built and tested.

The current canted blades should also have been tested with fences at additional pitches. Given the substantial reduction in optimal blade speed ratio with fences, it is possible that $\beta = -3.5°$ may not have been the optimal pitch with fences. Rather, it may have been closer to $\beta = -5.5°$ since with no fences the power performance at this pitch was close to the power performance with no fences at $\beta = -3.5°$ and it was shown that more outwards pitch may be beneficial at lower blade speed ratios. Geometry changes

(length, height, overhang, shape) to the fences may also provide additional benefit since the current fences were based on results from aircraft testing at somewhat higher speeds than the operational range of the turbine.

Any new set of canted blade should be designed to compare directly to a set of straight blades, as was the intention of the present work. Only with a set of canted blades and straight blades that operate at the same speed at peak power and have the same natural frequency can a conclusion be drawn on the extent to which excitation is reduced by canted blades.

Three dimensional simulations of canted blades would be very useful. The biggest obstacles are the computational power, system memory and time required to perform these very large simulations. Results from the present tests will be useful in validating such a model.

Another interesting change is modifying the sweep angle. Early NACA testing showed that lift coefficients were slightly higher at certain wing stations at $\Lambda = 30°$ sweptback wings than for unswept wings and wings swept at $\Lambda = 45°$.

REFERENCES

Allet A, Halle S, Paraschivoiu I. Numerical simulation of dynamic stall around an airfoil in Darrius motion. J. Solar Energy Engineering February 1999;121:69-76.

Armstrong S, Tullis S. Power performance of canted blades for a vertical axis wind turbine. J. Renewable and Sustainable Energy, 2011;3(1).

Armstrong S, Tullis S, Stern M. Canted blades for a vertical axis wind turbine. United States Provisional Patent Application Serial No. 61/310,970, 2010.

Blackwell B F, Sheldahl R E, Feltz L V. Wind Tunnel Performance Data for the Darrius Wind Turbine with NACA 0012 Blades. Sandia National Laboratories, SAND76-0130, 1976.

Bravo R, Tullis S, Ziada S. Performance testing of a small scale vertical-axis wind turbine. In: Proceedings of the 21st Canadian Congress of Applied Mechanics, Toronto, 2007.

Brochier G, Fraunie P, Beguier, Paraschivoiu I. Water channel experiments of dynamic stall on Darrieus wind turbine blades. AIAA J. Propulsion September-October 1986;2(5):445-59.

Cleary J W, Boddy L E. Wind-Tunnel Investigation of a 45° Sweptback Wing Having a Symmetrical Root and a Highly Cambered Tip, Including the Effects of Fences and Lateral Controls. National Advisory Committee for Aeronautics, NACA-RM-A53I21, November 1953.

Devaud C, Weisinger J, Johnson D, Weckman E. Experimental and numerical characterization of the flow field in the large-scale UW Fire Research Facility. Int'l J. Numerical Methods in Fluids June 2009;60(5):539-64.

Ferreira C J, Bijl H, van Bussel G, van Kuik G. Simulating dynamic stall in a 2D VAWT: Modeling strategy, verification and validation with particle image velocimetry data. J. Physics: Conference Series 2007a;75:012023.

Ferreira C J, van Bussel G, van Kuik G. 2D CFD simulation of dynamic stall on a vertical axis wind turbine: verification and validation with PIV measurements. In: 45th AIAA Aerospace Sciences Meeting and Exhibit/ASME Wind Energy Symposium, Reno, 2007b; 16191-16201.

Ferreira C J, van Bussel G, Scarano F, van Kuik G. PIV Visualization of Dynamic Stall VAWT and Blade Load Determination. In: 46th AIAA Aerospace Sciences Meeting and Exhibit, Reno, 2008; 1-13.

Ferreira C J, van Bussel G, van Kuik G, Scarano F. Visualization by PIV or dynamic stall on a vertical axis wind turbine. Experiments in Fluids 2009;46:97-108.

Fiedler A. Blade Pitch & Offset on a Vertical Axis Wind Turbine. McMaster University, Hamilton, ON. 2009.

Fiedler A, Tullis S. Blade offset and pitch effects on a high solidity vertical axis wind turbine. Wind Engineering May 2009;33(3):237-46.

Fujisawa N, Shibuya S. Observations of dynamic stall on Darrieus wind turbine blades. J. Wind Engineering and Industrial Aerodynamics 2001;89(2):201-14.

Gorlov A. Unidirectional helical reaction turbine operable under reversible fluid flow for power systems. United States Patent No. 5,451,137, 1995.

Hamada K, Smith T, Durrani N, Qin N, Howell R. Unsteady flow simulation and dynamic stall around vertical axis wind turbine blades. 46th AIAA Annual Aerospace Meeting and Exhibit 2008; 1-11.

Hansen M, Soresen D. CFD model for vertical axis wind turbine. In: Wind Energy for the new Millennum – Proceedings of the European Wind Energy Conference, Copenhagen, 2001.

Hirsch C, Mandal A. Flow curvature effect on vertical axis Darrieus wind turbine having high chord-radius ratio. European Wind Energy Conference October 22-26 1984, Hamburg. 405-10.

Holmes, J. Wind Loading of Structures. New York: Spon Press, 2003.

Howell R, Qin N, Edwards J, Durrani N. Wind tunnel and numerical study of a small vertical axis wind turbine. J. Renewable Energy February 2010;33:412-22.

Klimas P, Worstell C. Effects of blade preset pitch/offset on curved-blade Darrieus vertical axis wind turbine performance. Sandia National Laboratories, SAND-81-1762, October 1981.

Letko W, Goodman A. Preliminary Wind-Tunnel Investigation at Low Speed of Stability and Control Charateristics of Swept-Back Wings. National Advisory Committee for Aeronautics, NACA-TN-1046 1946.

Mandal A, Burton J. The effects of dynamic stall and flow curvature on the aerodynamics of Darrieus turbines applying the cascade model. Wind Engineering 1994;18:267-82.

Mclaren K, Tullis S, Ziada S. CFD Simulation of dynamic thrust and radial forces on a vertical axis wind turbine blade. 15th Annual Conference of CFD Society of Canada, 2007.

Mclaren K, Tullis S, Ziada S. Computational fluid dynamics simulation of the aerodynamics of a high solidity, small scale vertical axis wind turbine. Submitted to Wind Energy 2009. (Manuscript #WE-09-0114)

McLaren K, Tullis S, Ziada S. Vibration response behaviour of a high solidity, low rotational velocity, vertical axis wind turbine. 7th International Symposium on Fluid-Structure Interactions, Flow-Sound Interactions, and Flow-Induced Vibration and Noise / ASME 3rd Joint US-European Fluids Engineering Meeting, 2010.

Migliore P, Wolfe W, Fanucci J. Flow curvature effects on Darrieus turbine blade aerodynamics. J. Energy March-April 1980;4(2):49-55.

Newman, B G. Actuator-disc theory for vertical-axis wind turbines. Journal of Wind Engineering and Industrial Aerodynamics 1983;15:347-55

Paraschivoiu I. Double-multiple streamtube model for Darrieus wind turbines. In: Second DOE/NASA Wind Turbine Dynamics Workshop, 1981, NASA CP-2185 19-25.

Paraschivoiu I, Delclaux F. Double-multiple streamtube model with recent improvements. AIAA Journal of Energy May-June 1983;7:250-5.

Paraschivoiu I, Allet A. Aerodynamic analysis of the Darrieus wind turbines including dynamic stall. J. Propulsion and Power 1988;4(5):472-7.

Paraschivoiu I, Beguier C. Visualization, measurements and calculations of dynamic stall for a similar motion of VAWT. In: Proceedings of the European Wind Energy Conference, Herning, 1998.

Paraschivoiu I. Wind Turbine Design – With Emphasis on Darrieus Concept. Polytechnic International Press, 2002.

Purser P E, Spearman M L. Wind-Tunnel Tests at Low Speed of Swept and Yawed Wings Having Various Planforms. National Advisory Committee for Aeronautics, NACA-TN-2445, December 1951.

Quiejo M, Jaquet B, Wolhart W. Wind-tunnel investigation at low speed of the effects of chordwise wing fences and horizontal-tail position on the static longitudinal stability characteristics of an airplane model with a 35° sweptback wing. National Advisory Committee for Aeronautics, NACA-TR-1203 1954.

St. Hilaire A, Carta F, Fink M, Jepson W. The influence of sweep on the aerodynamic loading of an oscillating NACA 0012 airfoil. Volume 1: Technical report. National Aeronautics and Space Administration, NASA-CR-3092 1979.

Shaughnessy E, Katz I, Schaffer J. Introduction to Fluid Mechanics. New York: Oxford University Press, 2005.

South P, Rangi R. An Wind Tunnel Investigation of a 14ft. Diameter Vertical Axis Windmill. National Aeronautical Establishment. LTR-LA-105 1972.

Strickland J. The Darrieus Turbine: A Performance Prediction Model Using Multiple Streamtube. Sandia National Laboratories, SAND75-0431, October 1975.

Strickland J, Webster B, Nguyen T. A vortex model of the Darrieus turbine: An analytical and experimental study. J. Fluids Engineering 1979;101:500-5.

van Kuik, G A M. The Lanchester-Betz Joukowsky Limit. Wind Energy 2007;10(3):289-91.

Weisinger, J. Characterization of the University of Waterloo Live Fire Research Facility wind generation system. University of Waterloo, Waterloo, ON. 2004.

APPENDIX A: AIRFOIL AND BLADE FENCE COORDINATES

Table A-1: Airfoil coordinates for NACA 0015 straight blade based on a 450mm chord terminated at 420mm ("c" is 450mm). Radius at the trailing edge is 0.00889c.

x/c	y/c
0	0
0.0125	0.02367
0.0250	0.03268
0.0500	0.04443
0.0750	0.05250
0.1000	0.05853
0.1500	0.06682
0.2000	0.07172
0.2500	0.07427
0.3000	0.07502
0.4000	0.07200
0.5000	0.06617
0.6000	0.05704
0.7000	0.04580
0.8000	0.03279
0.8778	0.02150
0.8933	0.01822
0.9089	0.01411
0.9244	0.00944
0.9282	0.00806
0.9333	0

Table A-2: Blade fence coordinates

x/c	y/c
-0.025	0
-0.025	0.033
0.000	0.053
0.025	0.04
0.075	0.043
0.150	0.048
0.250	0.048
0.350	0.048
0.450	0.045
0.550	0.043
0.650	0.035
0.700	0.025
0.750	0

APPENDIX B: ERROR CALCULATIONS

B.1 POWER COEFFICIENT REPEATABILITY

Figure B-1 shows the power performance results of testing the turbine with three NACA 0021 blades with and without cables attached to the top of the shaft. Aside from the cables, there were no other differences between the two tests and therefore the repeatability of the testing procedure can be determined by analyzing the results.

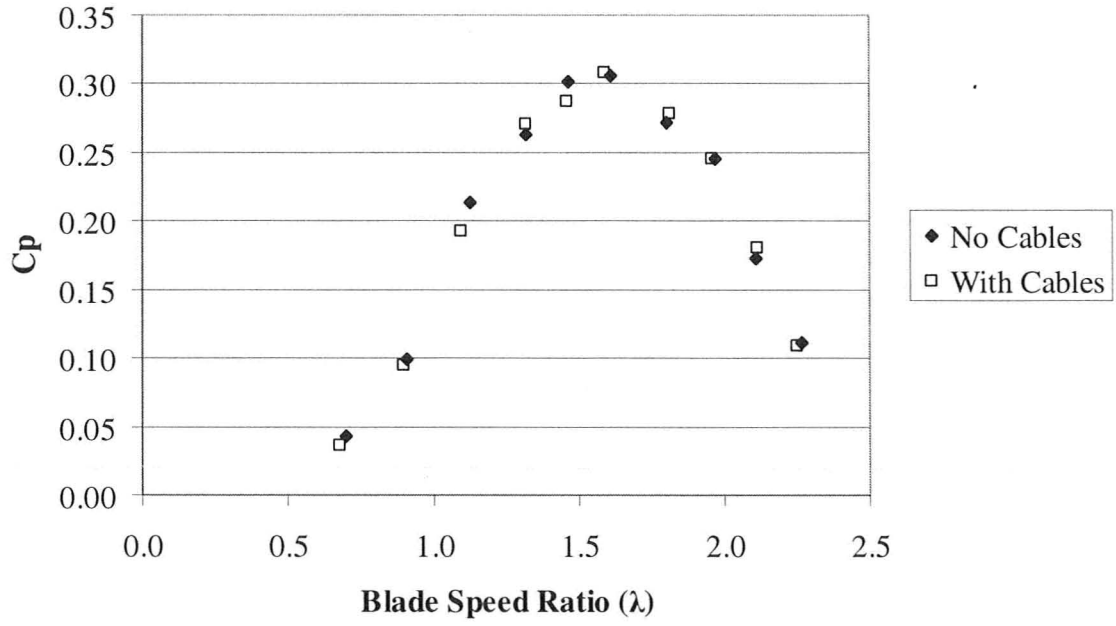

Figure B-1: Power coefficient curves for NACA 0021 blades tested with and without cables attached to the top of the shaft at 8 m/s wind speed.

Table B-1 shows the power coefficient data for figure B-1. The points at $\lambda = 1.1$ have been omitted since the curve is steep at this location and the blade speed ratios do not match well. The standard deviation in the power coefficients is $\sigma_{Cp} = 0.007$. Therefore, the power coefficients are repeatable to 95% within a range of $\Delta C_P = +/-0.014$

assuming a normal distribution. This is likely an overestimate of the repeatability error since the blade speed ratios do not match exactly and therefore some differences in power coefficients should be expected.

Table B-1: Power coefficients and variances for 3 NACA 0021 blades with and without cables

C_P No Cables	λ No Cables	C_P With Cables	λ With Cables	Mean	Variance
0.04	0.70	0.04	0.68	0.04	0.00004
0.10	0.90	0.09	0.90	0.10	0.00002
~~0.21~~	~~1.12~~	~~0.19~~	~~1.09~~	~~0.20~~	~~0.00043~~
0.26	1.32	0.27	1.32	0.27	0.00006
0.30	1.46	0.29	1.46	0.29	0.00020
0.31	1.61	0.31	1.59	0.31	0.00001
0.27	1.80	0.28	1.81	0.28	0.00005
0.25	1.97	0.25	1.96	0.25	0.00000
0.17	2.11	0.18	2.12	0.18	0.00006
0.11	2.26	0.11	2.25	0.11	0.00001

B.2 Load Cell Calibration and Accuracy

Figure B-2 shows a typical load cell calibration. At peak power for canted blades, the average output voltage of the load cell is roughly 0.8V, 1.05V and 1.65V at 8 m/s wind speed, 9 m/s wind speed and 10 m/s wind speed respectively. At these values, the maximum differences between the "Loading+Unloading" best fit line and the "Loading" or "Unloading" data are 38% for 8 m/s, 28% for 9 m/s and 18% for 10 m/s. The large error at 8 m/s is due to the low voltage which is affected significantly by the intercept of the best fit line used since the displacement of the lines is roughly equal over the entire calibration range. These error values represent the worst case scenario (approximately three standard deviations) and reporting these values would significantly overstate the error. It is more realistic to account for two standard deviations which would account for

95% of the measurements. The error at two standard deviations is 25% at 8 m/s, 19% at 9 m/s and 12% at 10 m/s wind speed.

The fit of the "Loading" and "Unloading" lines individually is much better. A dynamic calibration procedure would improve the measurement accuracy greatly since a dynamic calibration would be more representative of how the apparatus behaves during operation. It would however be difficult to apply a constant measureable force (torque) to the turbine causing it to rotate at a constant rate.

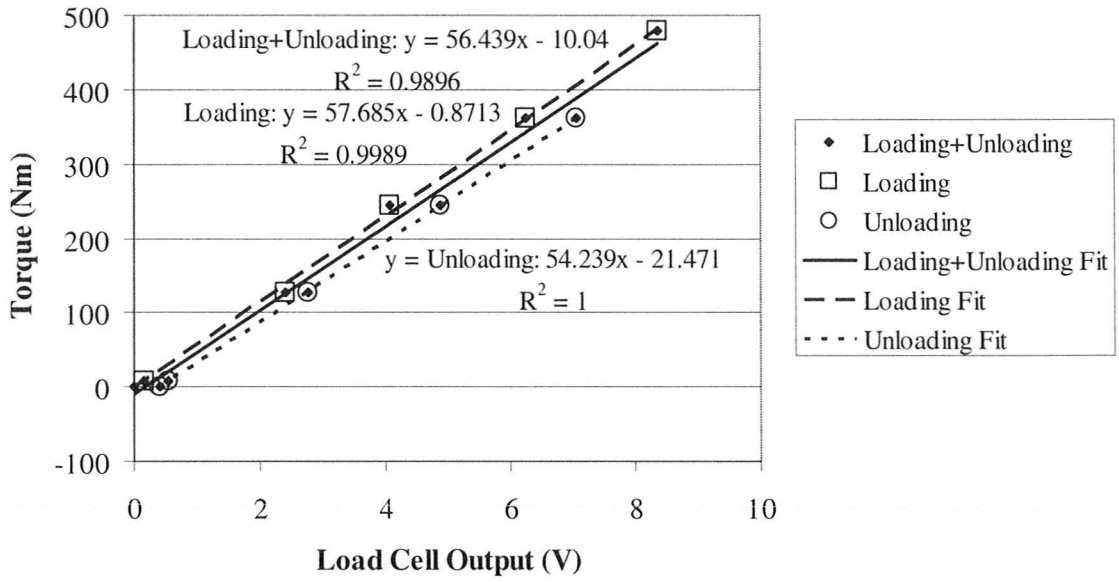

Figure B-2: Typical load cell calibration. The load cell was calibrated by statically clamping the brake disc with the calliper as it rested against the load cell and incrementing the torque by applying known tangential forces at the end of a strut.

B.3 Anemometer Placement and Accuracy

Figure B-3 shows time averaged wind speed profiles of the Waterloo Live Fire Research Facility (Weisinger, 2004) with no flow obstructions. The anemometer was located 3.8m downstream of the plenum chamber exit which is between Figure B-3(a)

and Figure B-3(b) and is shown as a black dot. The turbine was located 8m from the plenum exit which is between Figure B-3(b) and Figure B-3(c).

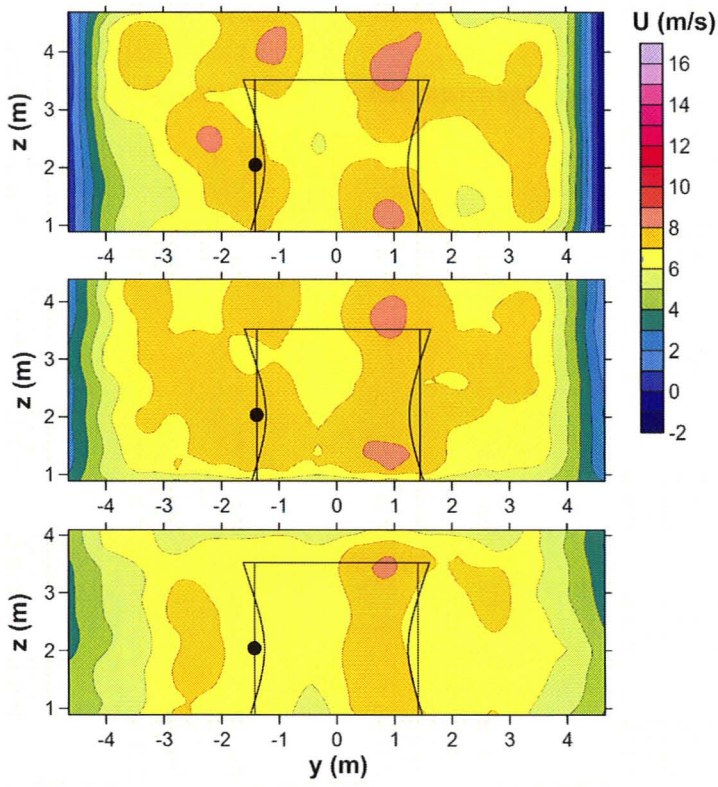

Figure B-3: Time averaged wind speed profiles at the University of Waterloo Live Fire Research Facility (top) 2m, (middle) 5m and (bottom) 11m downstream of the plenum chamber exit. Average wind speed is approximately 7 m/s where the turbine sits. The outline of the canted blade and straight blade turbines are shown as well as a black dot to represent the location of the anemometer. (Weisinger, 2004)

Without wind speed contours at the turbine and anemometer locations, the spatially averaged wind speed experienced at the turbine and the point speed at the anemometer can only be estimated relative to the average wind speed. With this in mind, the average wind speed experienced by the turbine would be approximately 7 m/s if the effect of the turbine on the upstream flow speed is ignored. The contours suggest that there would be little difference in the average flow speed experienced by canted blades compared to straight blades. The anemometer would measure a wind speed at maximum

about 0.5m/s higher than the average wind speed experienced by the turbine which is the approximate absolute error in the wind speed measurement due to anemometer placement.

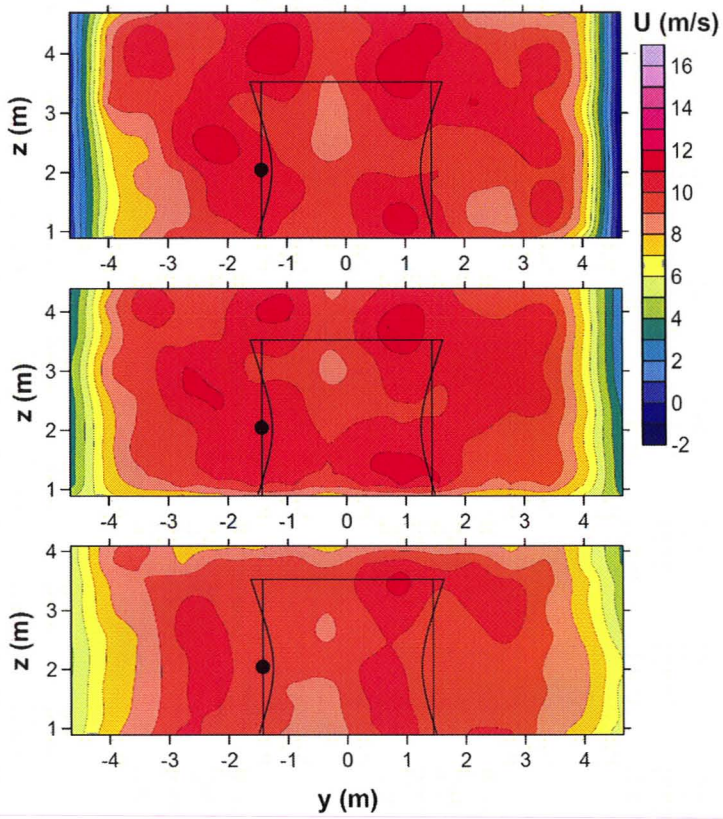

Figure B-4: Time averaged wind velocity profiles at the University of Waterloo Live Fire Research Facility (top) 2m, (middle) 5m and (bottom) 11m downstream of the plenum chamber exit. Average wind speed is approximately 9m/s where the turbine sits. The outline of the canted blade and straight blade turbines are shown as well as a black dot to represent the location of the anemometer. (Weisinger, 2004)

Figure B-4 shows similar unobstructed time averaged wind speed profiles at higher wind speeds (Weisinger, 2004). There is more spatial variation in the wind speed than at the lower speed. The average wind speed experienced by the turbine would be approximately 9m/s neglecting any effect of the turbine on the flow. There appears to be

a difference in measured wind speed of up to 1 m/s due to anemometer placement compared to the average speed experienced by the turbine.

Other wind speed contour plots suggest that the difference maximum between the measured wind speed and the average wind speed at the turbine would be roughly 0.25 m/s at 3m/s average wind speed and 1.5 m/s as 12 m/s average wind speed. Considering the error at the various average wind speeds, the approximate errors in the wind speed measurement due to anemometer placement can be estimated to be +/-0.45 m/s at 6 m/s average wind speed, +/-0.75 at 8 m/s average wind speed and +/-1.2 m/s at 10 m/s wind speed. These are maximum estimates of the wind speed error and would account for 100% of the possible variation in the wind speed due to anemometer placement and as such would significantly overestimate the error. A more realistic approach would be to consider these errors as three standard deviations from the mean. Therefore, to within an accuracy of 95% assuming a normal distribution, the error can be stated as +/-0.3 m/s at 8 m/s wind speed, +/-0.5 m/s at 8 m/s and +/-0.8 m/s at 10 m/s.

This gives an error in wind power of 16% at 6 m/s average wind speed, 20% at 8 m/s wind speed and 26% at 10 m/s wind speed. Since the anemometer does not move during the tests, its placement has the same effect on all test cases at the same wind speed. The measurement error is in the anemometer itself is +/-1% in wind speed which corresponds to a 3% error in wind power. This is the relevant wind power error within the present tests.

B.4 Rotational Speed Error

The error in the measurement of rotation speed is less than 1%.

B.5 Overall Error

The overall error in the power coefficients is computed by adding the individual errors in quadrature. At 8 m/s for canted blades operating at peak power, the absolute error is:

$$Error = \sqrt{E_{WindPower}^2 + E_{LoadCell}^2 + E_{RPM}^2} = \sqrt{(20+3)^2 + 25^2 + 1^2} = 34\%$$

Similarly, the error for canted blades with fences operating at peak power in 10 m/s wind is:

$$Error = \sqrt{E_{WindPower}^2 + E_{LoadCell}^2 + E_{RPM}^2} = \sqrt{(26+3)^2 + 12^2 + 1^2} = 31\%$$

The error in the blade speed ratio at 8 m/s wind speed is:

$$Error = \sqrt{E_{WindSpeed}^2 + E_{RPM}^2} = \sqrt{6.3^2 + 1^2} = 6.3\%$$

Similarly, the error in the blade speed ratio at 10 m/s wind speed is:

$$Error = \sqrt{E_{WindSpeed}^2 + E_{RPM}^2} = \sqrt{8^2 + 1^2} = 8\%$$